Geochimica et Cosmochimica Acta xxx (xxxx) xxx

Contents lists available at ScienceDirect

Geochimica et Cosmochimica Acta

journal homepage: www.elsevier.com/locate/gca

# Co-evolution of organics and water in experimentally shocked Murchison and EET 90628 chondrites

E. Quirico [a,*], H. Yabuta [b], P. Beck [a], L. Bonal [a], A. Bardyn [c,e], L.R. Nittler [c,d], C.M.O'D. Alexander [c]

[a] Université Grenoble Alpes, CNRS, Institut de Planétologie et Astrophysique de Grenoble (IPAG), UMR 5274, Grenoble F-38041, France
[b] Graduate School of Advanced Science and Engineering, Hiroshima University, Hiroshima, Japan
[c] Earth and Planets Laboratory, Carnegie Institution for Science, 5241 Broad Branch Road, N.W., Washington, DC 20015, USA
[d] School of Earth and Space Exploration, Arizona State University, Tempe, AZ 85287, USA
[e] Brin Mathematics Research Center, The University of Maryland, 4146 CSIC Bldg. #406, 8169 Paint Branch Drive, College Park, MD 20742-3289, USA

ARTICLE INFO

Associate editor: Martin Robert Lee

*Keywords:*
Impact
Shock-recovery experiments
Insoluble organic matter

ABSTRACT

A significant population of primitive carbonaceous chondrites experienced short-duration heating, which is usually attributed to either impact or solar heating. Shock recovery experiments performed on carbonaceous chondrites have successfully reproduce the typical evolution in the petrographies and mineralogical compositions of natural samples. However, only few studies focused on the chemical and structural transformations of insoluble organic matter (IOM). We report here on shock recovery experiments conducted on two chondrites: Murchison (CM2) and Elephant Moraine EET 90628 (L3.0). Experiments on Murchison show carbonization and oxidation of IOM at all shock intensities (5–50 GPa) and a pronounced structural evolution at 40 GPa associated with complete dehydroxylation of serpentines, as well as formation of olivine and amorphous silicates. The δD value of Murchison IOM (initial $\delta D = 1636 \pm 529$ ‰) evolves significantly, with the rapid disappearance of isotopic hot spots and a bulk δD of −79 ‰ at 40 GPa. At 40 GPa, the extent of dehydroxylation of serpentines is consistent with stage III heated chondrites, but the structural characteristics of the IOM resembles material from stage II meteorites, i.e. a slight modification of the IOM in a matrix dominated by serpentines.

These experiments only partially reproduce the characteristics of natural samples, and they show that the IOM evolution in short-duration heated C2 chondrites is essentially controlled by the post-shock cooling episode, which lasts from hours to years, compared to $< \sim 1$ μs for the shock peak pressure. The high pressure conditions in the shock do not catalyze the carbonization process and the maturation of IOM. In contrast, the IOM evolution in heated C2 chondrites is better simulated by conventional heating experiments under controlled redox conditions over durations of hours. Shock recovery experiments, however, could be interesting to assess the effect of hypervelocity impacts by small impactors on the surface of airless bodies. Experiments performed on EET 90628 show a structural evolution consistent with natural objects. In particular, the co-evolution of the width and ratio of the peak intensities of the D-band (FWHM-D and $I_D/I_G$, respectively) in the Raman spectra of the IOM from the shocked samples is consistent with those measured on type 3 ordinary and carbonaceous chondrites. An interesting finding is that the G-band width and position parameters (FWHM-G and $\omega_G$) do not correlate with the shock intensity, just as these parameters do not correlate with the intensity of thermal metamorphism in the case of type 3 chondrites. This lack of correlation is not observed on Earth in the case of coals and kerogens that experienced a progressive thermal history.

## 1. Introduction

Collisions between planetary bodies played a major role in the formation and evolution of the Solar System. They allowed for the growth of the terrestrial planets, including the accretion of volatile elements such as noble gases, carbon (C), nitrogen (N), hydrogen (H) and a broad diversity of organic molecules (Chen et al., 2019; Lambrechts et al., 2019; Péron et al., 2018). Collisions also shaped the size distributions of

* Corresponding author.
*E-mail address:* eric.quirico@univ-grenoble-alpes.fr (E. Quirico).

https://doi.org/10.1016/j.gca.2025.05.046
Received 16 February 2025; Accepted 28 May 2025
Available online 1 June 2025

**Table 1**
Shock experiments parameters and analyses.

| Sample | Peak Pressure GPa | Flyer velocity km/s | Shock period µs | Total E J/g | Waste E J/g | Infrared | Raman |
|---|---|---|---|---|---|---|---|
| Murchison | 5 (6) | 0.40 | 0.48–0.96 | 175.3 | 34.3 | IOM/matrix | IOM/matrix |
| | 10 (10.4) | 0.65 | 0.40–0.80 | 397.8 | 80.9 | | |
| | 20 (19.5) | 1.10 | 0.35–0.70 | 937.3 | 207.8 | | |
| | 40 (39.2) | 1.91 | 0.29–0.58 | 2209.7 | 588.7 | | |
| | 50 (49) | 2.25 | 0.54–0.23 | 2861.4 | 829.7 | | |
| EET 90628 | 5 | n.d. | n.d. | n.d. | n.d. | n.d. | matrix |
| | 10 | n.d. | n.d. | n.d. | n.d. | n.d. | |
| | 20 | n.d. | n.d. | n.d. | n.d. | n.d. | |
| | 30 | n.d. | n.d. | n.d. | n.d. | n.d. | |
| | 40 | n.d. | n.d. | n.d. | n.d. | n.d. | |
| | 50 | n.d. | n.d. | n.d. | n.d. | n.d. | |

Total E: Total energy. Waste E: waste heat energy. Infrared: infrared analyses. Raman: Raman analyses. n.d.: not determined.

asteroids and trans-Neptunian objects, and have released fragments of these objects that can eventually hit the Earth to be recovered as meteorites or micrometeorites (Bottke et al., 2015; Stern and Kenyon, 2003). Insights into collisional processes are provided by meteorites, which record high pressure and temperature conditions in their petrological and mineralogical characteristics. Hypervelocity impacts generate shock waves that lead to textural transformation (fracturing, compaction, comminution), mineral deformation (undulatory extinction, mosaicism), melting and re-crystallization (maskelynite, and high-pressure minerals like ringwoodite). Based on such observations, different classification schemes have been proposed to reflect the intensity of the shock experienced by ordinary chondrites, classified from S1 to S6, with each stage being assigned a shock pressure value (Fritz et al., 2017; Hu and Sharp, 2022; Stöffler et al., 2018, 1991). By applying this scale to carbonaceous chondrites, Scott et al. (1992) found shock signatures in the range S1-S4 in 69 chondrites, and found that CM2 and CO3 groups are the least shocked (36 out of 38 were unshocked), while CV and CK are the most shocked. However, a large fraction of primitive CM, CR and C2-ungrouped carbonaceous chondrites show evidence of short-duration heating, which could be caused by hypervelocity impacts, though solar heating is another process that cannot be ruled out (Ikeda, 1992; Mahan et al., 2018; Matsuoka et al., 1996; Nakamura, 2005; Nakato et al., 2008; Quirico et al., 2018; Tomeoka, 1990; Tomeoka et al., 1989a, 1989b; Tonui et al., 2014, 2002, 2003; Wang and Lipschutz, 1998; Zolensky et al., 1989).

Shock recovery experiments are a powerful tool for studying the chemical and structural transformations of meteorites and their constituent materials. Many studies have focused on simple minerals and ordinary chondrites, and are able to explain the presence of melting veins, the formation of high-pressure minerals and the evolution of the cooler bulk host rock. Post-shock temperatures, Hugoniot curves or shock duration have also been determined (Fritz et al., 2017; Milton and DeCarli, 1989; Stöffler, 1972; Stöffler et al., 2018, 1991; Stöffler and Langenhorst, 1994). Shock recovery experiments that focused on primitive carbonaceous chondrites point to heating processes, volatile production due to serpentine dehydroxylation, and H and C isotopic evolution in organic matter in the case of the Murchison meteorite (Mimura et al., 2005; Nakamura, 2000; Tomeoka et al., 1999; Tomioka et al., 2007). However, no study to date has focused on the evolution of the structure and composition of insoluble organic matter (IOM) along with the co-evolution of minerals. Because IOM is a useful probe of the thermal history that is insensitive to retrograde modification, its study in artificially shocked samples could provide new tracers of the intensity of shock metamorphism. This is the aim of the study presented here, which focuses on a series of shock recovery experiments carried out on the Murchison (CM2) and Elephant Moraine (EET) 90628 (L3.0) chondrites in the pressure range of 5–50 GPa. Bulk samples and extracted IOM were characterized by infrared and Raman micro-spectroscopy, providing insight into the shock-controlled carbonization process. NanoSIMS (Nanoscale Secondary Ion Mass Spectrometry) measurements were also performed to provide insight into the hydrogen isotopic composition of the IOM at small scales. The results of these analyses were compared with those of natural samples, and we discuss the extent to which these experimental simulations are representative of natural conditions.

## 2. Samples and analytical methods

### 2.1. Samples

The shock experiments were conducted on two bulk rock chondrites: Murchison and EET 90628. The Murchison sample was provided by the Field Museum of Chicago. It is a type 2 CM chondrite that experienced moderate aqueous alteration among other CM chondrites (volume modal abundance of phyllosilicates 70 %, Howard et al., 2011), no short-duration heating in its parent body, and is assigned a 1.6 petrologic subtype (Alexander et al., 2013). EET 90628 was provided by the Antarctic Meteorites Working Group/JSC (Houston). It is a weakly thermally metamorphosed ordinary chondrite (L subgroup), with a petrologic type of 3.0 (Bonal et al., 2016). This assignment means that it is one of the least thermally processed type 3 chondrites, but its degree of heating is higher than that of Murchison. It is worth noting that a fraction of Type 1 and 2 chondrites have experienced a variety of heating in their parent bodies. However, the intensity of this heating is not reflected in their petrological types, which essentially reflect hydration, but by four stages from I to IV (Nakamura, 2005):

- stage I (<250 °C) refers to weakly heated chondrites, which show very weak modification of their mineralogical composition. Their matrix is dominated by phyllosilicates, and the main modifications are those observed in reflectance spectroscopy;
- stage II (250–500 °C) refers to chondrites that include a low degree of heating, and which have preserved most of their phyllosilicates (Miller Range, MIL, 07700) or whose mineralogy is dominated by amorphous silicates (e.g., Wisconsin Range, WIS 91600);
- stage III (500–750 °C) refers to chondrites that still contain amorphous materials, but include anhydrous minerals that formed from amorphous materials crystallization;
- (IV) stage IV (>750 °C) refers to chondrites composed of fully recrystallized amorphous materials and mineralogy is dominated by olivine and pyroxene.

The IOM-based classification proposed by Quirico et al. (2018) defines 3 groups, TI, TII, TIII/IV, which are consistent with the stages defined by Nakamura (2005), but do not strictly correspond to them. TII refers to chondrites that experienced a low degree of heating and includes objects without substantial decomposition of serpentine (e.g. MIL 07700) and objects equivalent to stage II containing abundant amorphous silicates (e.g. WIS 91600). TIII/IV are equivalent to stages III and IV, since the IOM structure indicates significant heating and chondrites contain crystalline silicates, but it does not allow to distinguish between

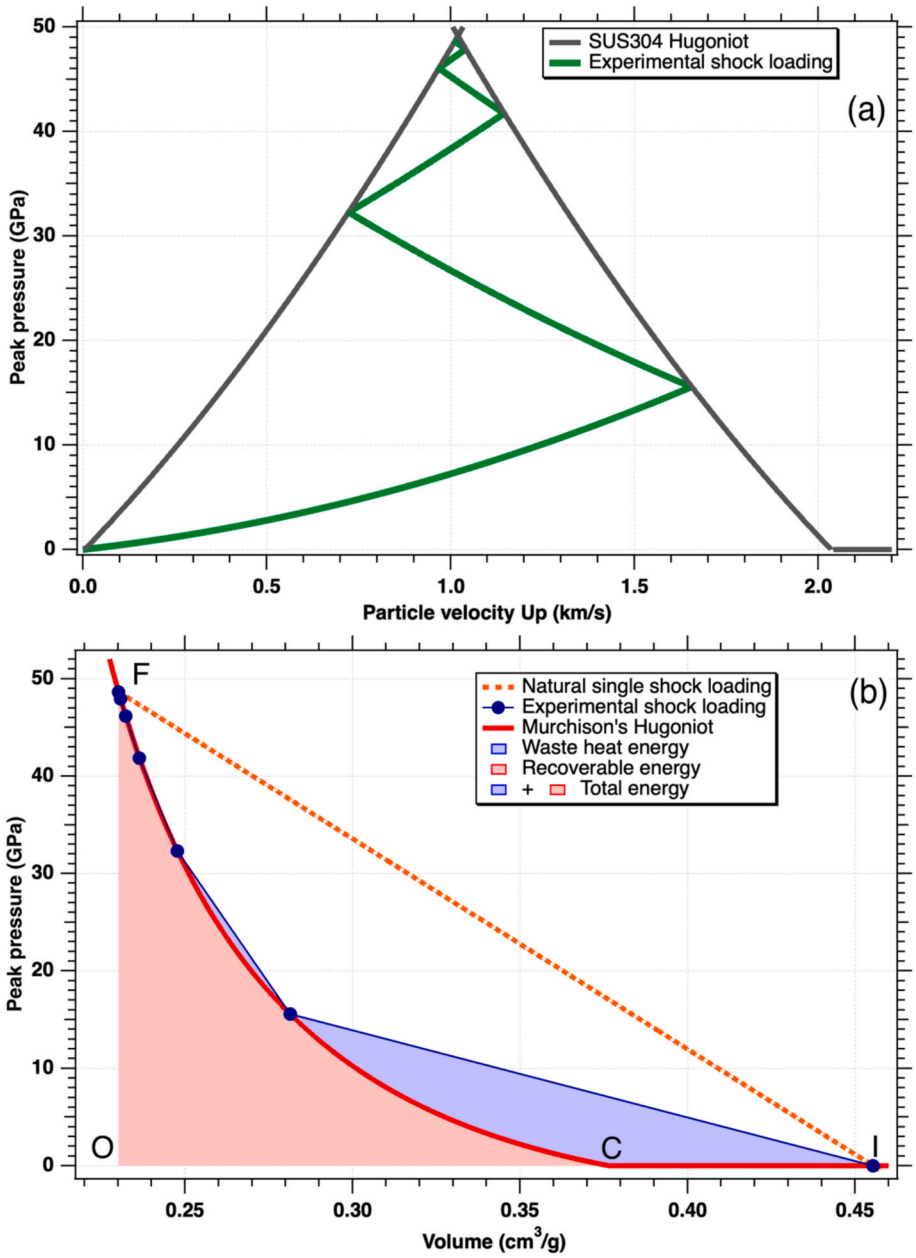


**Fig. 1.** (a) Multiple reflections at the boundaries between the Murchison sample and the SUS304 capsule. (b) Single loading shock (Rayleigh dotted line) and multiple reflections shock in the experimental set-up (blue line segments). The waste heat energy is calculated as the difference between the total energy and the recoverable energy (shaded in red), assuming that the release adiabat is given by the Hugoniot curve.

Nakamura's stages III and IV. However, this distinction can be made using infrared spectra of bulk samples.

### 2.2. Shock recovery experiments

The shock recovery experiments were conducted at the Tokyo Institute of Technology (Japan) in four sessions conducted between 2010 and 2016 (Table 1). The samples of bulk meteorites were ground and pressed into pellets (Ø 14 mm; 1 mm thick), which were individually encased into stainless steel (SUS304) recovery capsules (Atou et al., 2010; Hongo et al., 2007). For each experimental run, a capsule was inserted into a stainless steel sample container plugged to a momentum trap, and was impacted by a flyer accelerated with one- or two-stage light-gas guns. In the case of the experiments on the Murchison chondrite, we used flyers with 1–2 mm thick plates made of copper covering a range of velocity of 0.4–2.25 km.s$^{-1}$. A 5–50 GPa peak pressure range in the recovery capsule was achieved by combining different flyers with different velocities. The shocked state in the sample was considered to equilibrate with that of the capsule through multiple reflections at the capsule boundaries. The peak pressures (Table 1) were calculated with the impedance match method, using the measured impact velocity and the Hugoniot curves of the flyer plate material. The peak pressure values in the text are the calculated values rounded up or down to the nearest integral number. The pressure period reported in Table 1 corresponds to the duration of the pressure pulse, from the onset of the shock and the arrival of the rarefaction wave, i.e. the time of a round trip through the flyer plate (e.g. Mimura et al., 2003). The Hugoniot curves and shock EOS (Equation Of State) used for calculations were taken from Marsh, (1980) for SUS304, Mitchell and Nellis (1981) and Thomas et al. (2019) for ultrapure copper, Anderson and Ahrens (1998) for the Murchison chondrite.

Two methods have been used for determining the shock and post-

**Table 2**
Calculations of shock and post-shock temperatures.

| | | Single shock loading | | | | Experiment | | Experiment |
|---|---|---|---|---|---|---|---|---|
| | | Method A | | Method B | | Method B | | Tomioka07 |
| Sample | Peak Pressure GPa | Shock T (K) | Post-S T (K) | Shock T (K) | Post-S T (K) | Shock T (K) | Post-S T (K) | Shock T (K) |
| Murchison | 5 (6) | 410 | 300 | 889 | 627 | 486 | 343 | |
| | 10 (10.4) | 447 | 300 | 1397 | 918 | 610 | 401 | 336 |
| | 20 (19.5) | 597 | 359 | 2749 | 1636 | 941 | 560 | 642 (21 GPa) |
| | 40 (39.2) | 951 | 517 | 7095 | 3570 | 2272 | 1036 | 911 (36 GPa) |
| | 50 (49) | 1119 | 576 | 9245 | 4667 | 2649 | 1337 | 1377 |

Temperatures are derived using a specific heat Cv of 800 kJ.kg$^{-1}$.K$^{-1}$. Shock T: shock temperature. Post-S T: post-shock temperature. Method A consisted in numerically solving equation (1), while in Method B consisted the waste heat energy was determined from the P-V diagram (Fig. 1). Tomioka07: averaged shock temperature calculated in Tomioka et al. (2007) with the numerical code Autodyn 2D, rescaled with $C_v$ = 800 kJ.kg$^{-1}$.K$^{-1}$.

shock temperatures for the experiments on the Murchison chondrite. The first method (hereafter Method A) consisted in numerically solving the following equation, derived from the Rankine-Hugoniot 1D equations and the thermodynamic identity equation:

$$\frac{\partial T}{\partial V} = -\frac{T}{V}\gamma + \frac{1}{2C_v}\left[\frac{\partial P}{\partial V}(V_0 - V) + (P - P_0)\right] \quad (1)$$

The shock temperature was then calculated in the case of a single shock loading. Note that the experimental data points of the Hugoniot of Anderson and Ahrens (1998) were directly used in this calculation, instead of the fit based on an EOS model and which is relevant to a putative non-porous Murchison chondrite. Therefore, the simulation applies for a chondrite with a natural porosity of 16 %. The post-shock temperature was derived using only the first two terms of Equation (1) that are relevant to an adiabatic release. The Gruneisen parameter γ was set to 1 (Hugoniot of Anderson and Ahrens, 1998). The heat capacity $C_v$ was taken as 800 kJ.kg$^{-1}$.K$^{-1}$, assuming $C_v \sim C_p$ and taking the $C_p$ value from Opeil et al. (2020) and Piqueux et al. (2021). Considering that $C_v$ is constant over a wide temperature range is a questionable assumption, regarding the mineralogical and textural evolutions, in particular the phyllosilicates decomposition between 30 and 40 GPa. Unfortunately, very little thermodynamic data has been published.

The second method (hereafter Method B) is based on the determination of the waste heat energy through the measurements of specific areas in a P-V diagram of the Hugoniot (Fig. 1; Martinez et al., 1995; Stöffler, 1972; Tomeoka et al., 1999). The waste heat energy can be then converted in a post-shock temperature by dividing by $C_v$ in the case of a single shock loading. In the case of the experiments, the shock wave underwent multiple reverberations at the boundary of the surfaces of the sample and the SUS304 container. The (P,V) values of these reflections were determined through the impedance-match method and the waste heat energy and the post-shock temperature have been determined (Fig. 1). The shock temperature was finally determined by calculating an adiabatic compression. To illustrate this approach, Fig. 1a shows the multiple reflections within the 49 GPa sample in a P-Up diagram, while Fig. 1b illustrates the different area used to estimate the total energy and waste heat energy. In the single shock loading,which is more representative of the natural conditions, the compression follows the Rayleigh line, from the point I (Murchison with its natural porosity of ~ 15 %) to the point F. Assuming that the adiabatic decompression follows the Hugoniot curve, the total energy corresponds to the area of the IOF triangle and the recoverable energy is represented by the area shaded in red. In the experimental conditions, the total energy is bounded by the blue segments that correspond to the reverberation points mentioned above (Fig. 1a). In that case, the smaller amount of waste heat energy leads to lower temperatures, and in this respect the peak temperature is underestimated with respect to natural conditions. Note that the porosity of our samples was not measured, and it is possible that the real porosity exceeds that of the natural sample. This increase of porosity would result in an increase of the shock and post-shock temperatures.

The waste heat energy calculated for a single loading shock and multiple reverberations are basically in agreement with the results obtained by Tomeoka et al. (1999) (Table 1, see their Table 3). The differences between the two sets of results are primarily attributable to a shift in their V values of Murchison's Hugoniot (see their figure 16 versus Fig. 3 in Anderson and Ahrens (1998)). In the case of the single shock loading, the shock and post-shock temperatures are much higher for Method B with respect to Method A (Table 2). This difference can be primarily due that release adiabats are approximated by the Hugoniot curves (Martinez et al., 1995).

Tomioka et al. (2007) report estimations of shock temperatures using the numerical code Autodyn 2D, with the shock EOS from Anderson and Ahrens (1998), $C_v$ = 500 kJ.kg$^{-1}$.K$^{-1}$ (Matsui and Osako, 1979) and a Gruneisen parameter equal to 1. The study of Matsui and Osako (1979) was focused on ordinary chondrites, and is not relevant to CM chondrites. Recalculating the shock temperature with $C_v$ = 800 kJ.kg$^{-1}$.K$^{-1}$, we observe that our shock temperatures are larger by factor 1.8–3.1. As mentioned above, the approximation of the release adiabat with the Hugoniot curve explains, at least partly, an overestimation of the derived temperatures. As presented below, the analysis of the shocked samples reveals a major decomposition of phyllosilicates at 40 GPa, which is consistent with the two sets of results, as phyllosilicates decompose between 400 and 770 °C (Garenne et al., 2014). To say that no firm conclusions can be derived from these analyses. To sum up, our estimates of the shock and post-shock temperatures in our shock experiments are overestimated and the measurements of Tomioka et al. (2007) corrected with $C_v$ = 800 kJ.kg$^{-1}$.K$^{-1}$ are likely more realistic: 63 °C at 10 GPa; 370 °C at 21 GPa; 638 °C at 36 GPa; 1104 °C at 49 GPa.

### 2.3. Insoluble Organic Matter extraction

Insoluble Organic Matter of shocked Murchison samples was extracted at Osaka University using the CsF/HCl technique developed by Cody et al. (2002). Bulk chondrite samples were first crushed by hand in an agate mortar and transferred into Teflon tubes, where extraction of soluble organics was performed with water and chloroform/methanol (2/1 v/v). The samples were then treated with 2 N HCl to remove metals, carbonates and most sulfides. They were then mixed with dioxane and an aqueous CsF-HF solution with a concentration of 1.6 g/mL and pH 5–6, and shaken continuously for at least 12 h. Two distinct phases eventually separated: the dense unreacted mineral solids settled in the bottom of the tube, while the hydrophobic IOM was collected at the interface of the two immiscible liquids. The organic residues were pipetted off and rinsed several times in 2 N HCl, dioxane and milliQ water before drying at room temperature. All operations were performed under ambient conditions.

### 2.4. Raman micro-spectroscopy

Raman micro-spectroscopy was performed at Laboratoire de

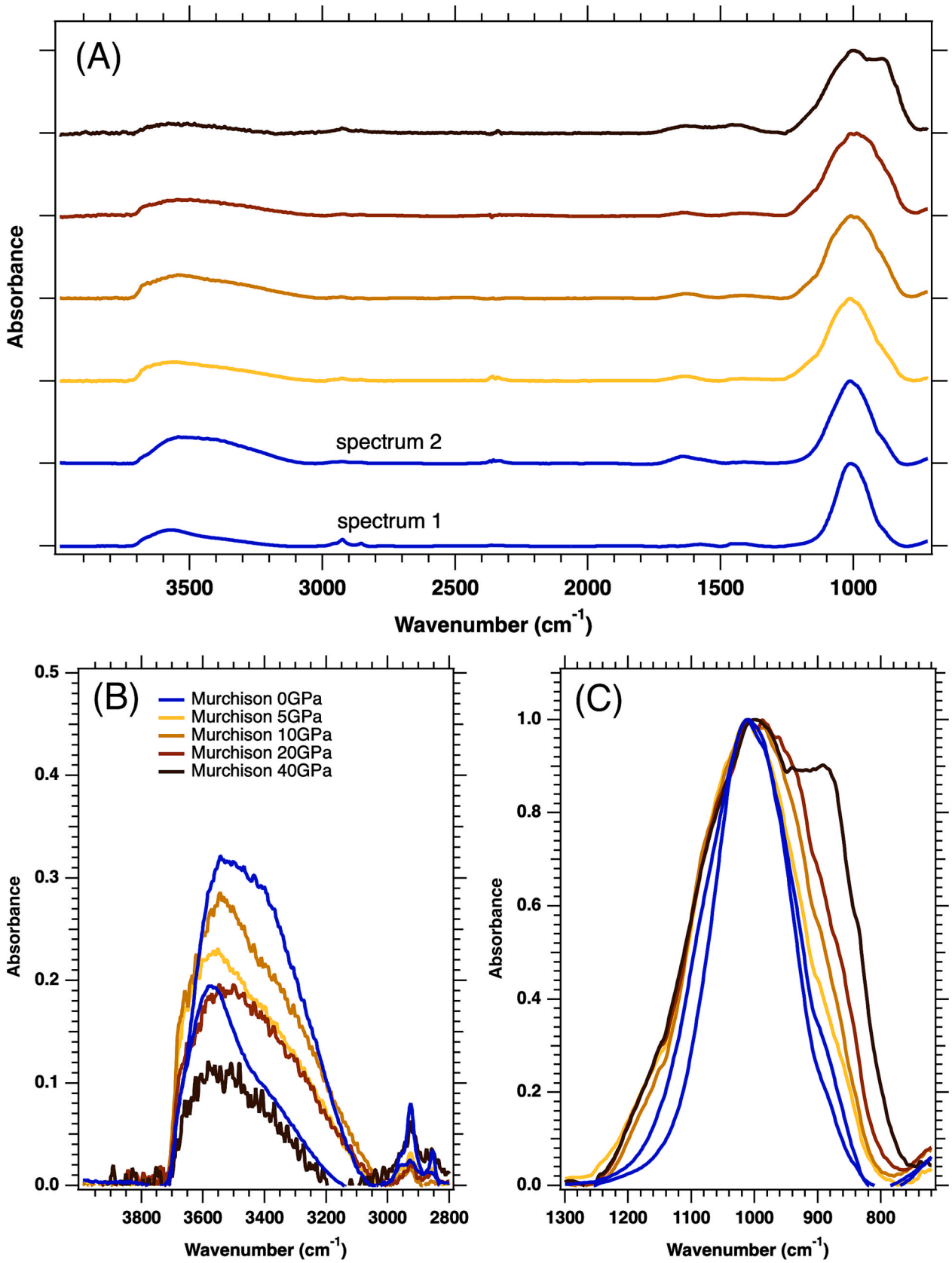


**Fig. 2.** Infrared spectra (baseline corrected) of matrix grains of Murchison shocked at 0, 5, 10, 20 and 40 GPa. The two spectra of unshocked Murchison show complete (spectrum 1) and partial removal (spectrum 2) of adsorbed molecular water.

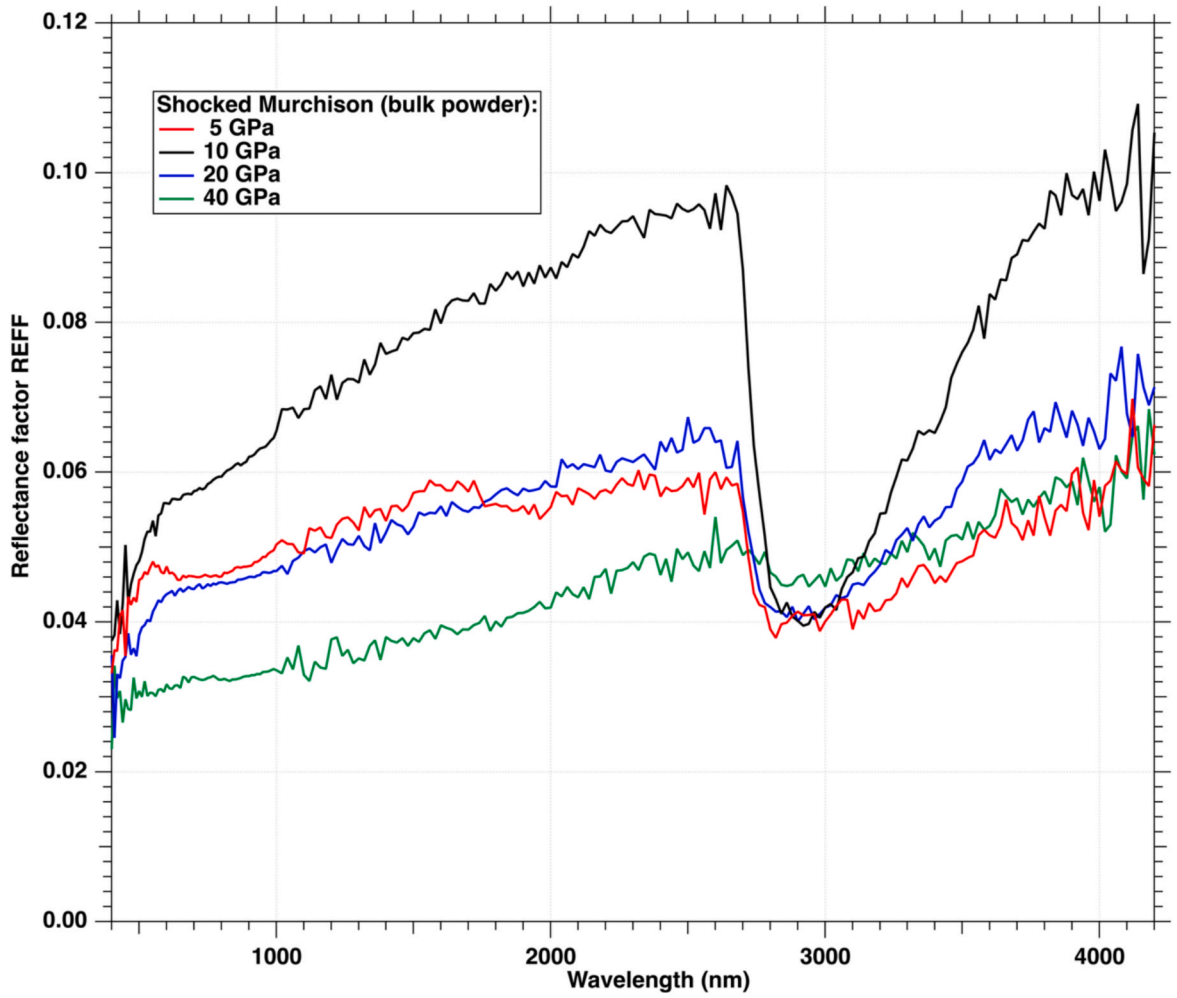


**Fig. 3.** Reflectance spectra of Murchison samples shocked at 5, 10, 20 and 40 GPa. A dramatic drop of the water band at ~ 3000 nm is clearly observed.

Géologie de Lyon Terre Planètes Environnement (LGLTPE: Université Claude Bernard – Ecole Normale Supérieure de Lyon, France). We used a LabRam Raman spectrometer (Horiba Jobin-Yvon) equipped with a 600 gr/mm grating and a Spectra Physics $Ar^+$ laser providing a 514 nm excitation wavelength. The laser beam was focused through a 100x objective resulting in a ~0.9 μm circular spot. Typical power on the sample and acquisition time were 300 μW and 90 s for raw matrix grains, and 50 μW and 90 s for IOM grains. Spectra were acquired in the 490–2230 $cm^{-1}$ spectral range. Measurement conditions were kept strictly constant to improve measurement reproducibility.

The Raman spectra were selected and numerically analyzed following the procedures detailed in Quirico et al. (2014, 2018). In short, the Raman spectra of the samples consist of broad first-order carbon bands (the so-called G and D bands or peaks), superimposed on a fluorescence background of variable intensity. We first selected by visual analysis the spectra that exhibited the highest Raman/fluorescence ratios and good signal-to-noise ratios. The Raman bands were extracted by subtracting the fluorescence background, assuming a linear shape within the 800–2000 $cm^{-1}$ range. We then applied a so-called Lorentzian-Breit-Wigner-Fano (LBWF) fit to the selected spectra (Eq. (2):

$$I(\omega) = I_G \frac{\left[1 + 2(\omega - \omega_G^p)/(Q.FWHM_G)\right]^2}{1 + \left[1 + 2(\omega - \omega_G^p)/FWHM_G\right]^2} + \frac{I_D}{1 + 4(\omega - \omega_D)^2/FWHM_D{}^2} \quad (2)$$

where $\omega_G = \omega_G^p + FWHM_G/2Q$, $FWHM_G$ and $FWHM_D$ are the full width at half maximum of the G and D bands, Q is the BWF coupling factor (it tends to infinity for a Lorentzian profile), and $\omega_D$ and $\omega_G^p$ are the pulsations. The Raman parameters that are used below are the peak positions $\omega_D$ and $\omega_G$, the ratio of the peak intensities of the D and G bands, respectively, and $FWHM_G$ and $FWHM_D$. Raman spectra are available in the SSHADE database (https://www.sshade.eu/) (Quirico and Bonal, 2010).

### 2.5. Infrared microscopy and reflectance spectroscopy

Infrared spectra were collected with a Bruker Hyperion 3000 infrared microscope at IPAG (Grenoble – France) and are available in the SSHADE (Quirico, 2010). The IR beam was focused through a 15x objective and the typical size of the spot on the sample was 50×50 $\mu m^2$. Spectra were measured at 4 $cm^{-1}$ spectral resolution with a MCT detector cooled with liquid nitrogen. The spectral range was 4000–650 $cm^{-1}$. IOM or raw matrix grains (typical size ~50 μm) were manually picked with a tungsten needle and transferred onto a 3x0.5 mm diamond window (type IIa synthetic diamond). The grains were then crushed with another diamond window, and the window containing the most crushed grains with optimal shapes was selected. The measurements were collected through an environmental cell operating under secondary vacuum while heating the samples at ~80 °C, removing as much as possible adsorbed atmospheric water.

Reflectance spectra of shocked samples were collected with the SHADOWS spectro-gonio-radiometer (Potin et al., 2018). The spectral spacing was 20 nm, and measurements were collected using an environmental cell operating under vacuum in order to remove adsorbed

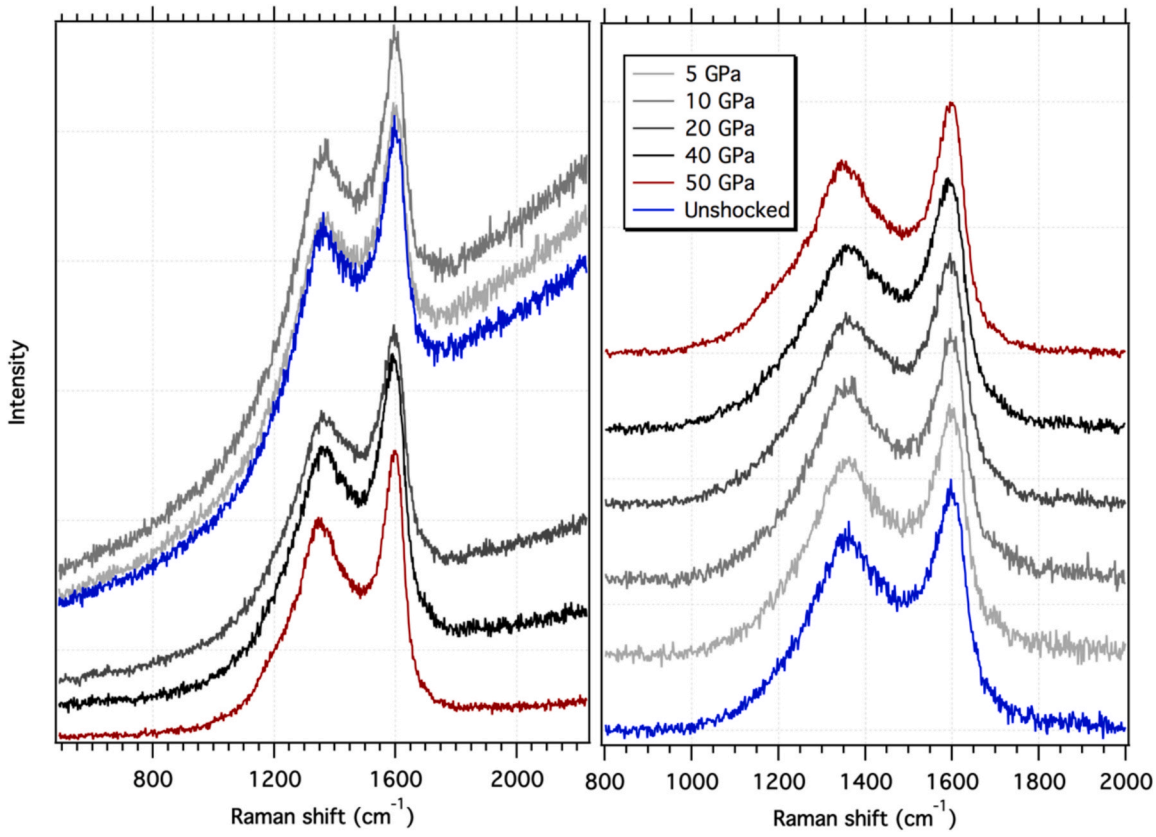


**Fig. 4.** Raman spectra of matrix grains from shocked Murchison samples collected with 514 nm excitation. Left: raw data. Fluorescence decreases as the peak pressure of the shock increases. Right: baseline corrected and normalized spectra. The spectral variations are weak for naked eye observation.

terrestrial water. Due to the low amount of sample, the size of the spot was limited to 1.2 mm. Raman and infrared spectra are available in the SSHADE database (https://www.sshade.eu/) (Quirico and Bonal, 2010; Beck and Potin, 2010).

### 2.6. NanoSIMS

H isotopic data were acquired on Murchison IOM with the Cameca NanoSIMS 50L at the Carnegie Institution. Small (10 s of μm) IOM fragments were first pressed into a clean Au foil with a sapphire disk. A ~ 10 pA primary $Cs^+$ ion beam with a diameter of a few 100 nm was rastered over the fragments and negative secondary ions of $^1H$, $^2H$, and $^{12}C^1H$ were collected in multicollection imaging mode. Each measurement consisted of 15 repeated frames of 262 s acquisition time each. The isotopic images were analyzed with the L'image software (L. Nittler). Following pixel-by-pixel correction for detector deadtime, the individual image frames were automatically co-aligned and summed to produce $^2H/H$ ratio images. Bulk D/H ratios for individual fragments were calculated by summing the counts over all pixels with $^1H^-$ intensity higher than 5 % of the maximum value of the image. An in-house organic standard was used to correct the data for instrumental mass fractionation.

### 2.7. Scanning transmission X-ray microscopy (STXM) – X-ray absorption near edge structure (XANES)

C-XANES spectra of the IOM particles were acquired by STXM-XANES at the beamline (BL) 5.3.2.2 of the Advanced Light Source (ALS) at the Lawrence Berkeley National Laboratory (Kilcoyne et al., 2003). The beamline employs a bending magnet providing a useful photon range spanning 250 to 800 eV with a flux of $10^7$ photons per second. Energy selection on BL5.3.2 is performed with a low-dispersion spherical grating monochromator and affords an energy resolution (E/ΔE) of 5000. Carbon-XANES transmission spectra were obtained in the stack scan mode with 0.1-eV resolution across the near edge region and 0.5-eV resolution below and above the near edge absorption. Energy calibration was conducted by measuring $CO_2$ gas prior to the measurements. The absorption spectra (optical density, OD) were obtained as $OD = -\ln(I/I_0)$, where I is the X-ray intensity transmitted from sample and $I_0$ is that recorded without sample. Cody et al. (2008) were referred to for the absorption peak assignment.

## 3. Results

### 3.1. Shock experiments on bulk Murchison

Pellets made of bulk Murchison powder were shocked at 5, 10, 20 and 40 GPa (first session), and 20 GPa and 50 GPa (second session). Matrix grains picked from the bulk samples were analyzed by transmission infrared micro-spectroscopy for the samples of the first session (Fig. 2). The spectra display the typical features observed for unheated carbonaceous chondrites (Beck et al., 2014, 2010). We observe a feature at ~1000 $cm^{-1}$ (hereafter, SiO band), controlled by the stretching mode of $SiO_4^{4-}$ tetrahedra. In the case of unheated CM chondrites, this feature is narrow and fairly symmetric, and it points to the presence of disordered serpentines (lack of long-range crystalline order). A broad feature is observed in the range 3700–3000 $cm^{-1}$, which is controlled by the stretching mode of OH groups trapped in the octahedral layer of serpentines, and by adsorbed molecular water trapped in closed porosity. The band at ~1640 $cm^{-1}$ is due to the bending vibration mode of $H_2O$, and is a probe of molecular water. Two spectra of the unshocked Murchison matrix are displayed in Fig. 2. They correspond to a full removal (spectrum 1) and a partial removal (spectrum 2) of adsorbed molecular water. The presence of molecular water makes it difficult to

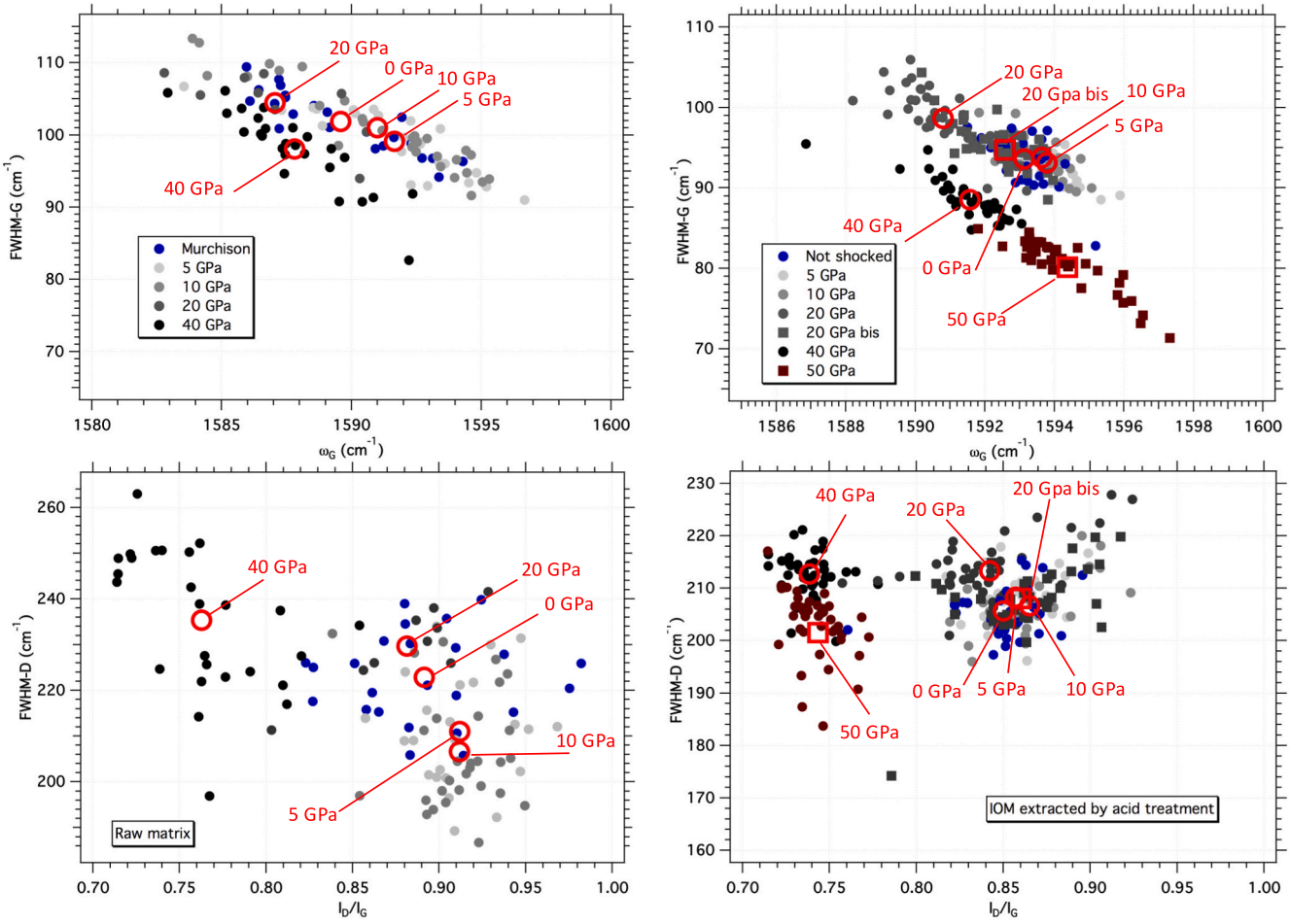


**Fig. 5.** Raman parameters of shocked Murchison samples derived from measurements on bulk samples (left) and IOM samples (right).

assess the OH abundances. Lastly, faint features are observed at 2964, 2925 and 2856 cm$^{-1}$, due to the symmetric and antisymmetric stretching modes of the $CH_2$ and $CH_3$ groups.

Upon increasing the peak pressure, we observe a dramatic evolution between 20 and 40 GPa. At 40 GPa, the OH/$H_2O$ abundance is much lower by a factor of 2–3 compared to the unshocked Murchison samples. The shape of this band displays variations from one grain to another, but it is quite rounded and shows evidence for considerable serpentine decomposition (lack of OH groups). The SiO band gets broader and displays a new structure, pointing to the appearance of features of new silicates: the SiO band of olivine (peaks at 832, 889 and 995 cm$^{-1}$), and amorphous materials (a broad and unstructured feature). In the range 0–20 GPa, the variations in the integrated intensities of the OH/$H_2O$ band reflect the intrinsic matrix heterogeneity and the partial removal of molecular water. Some mild mineralogical transformations are, however, suggested by the broadening and the shift of the SiO band from ~1014 to 990 cm$^{-1}$ at 20 GPa (Fig. 2).

The reflectance spectra collected on the bulk samples are displayed on Fig. 3. The main feature is the broad water band at ~3100 cm$^{-1}$, which comprises contributions from hydroxyl and molecular water trapped in serpentines, and presumably amorphous silicates in the 40 GPa sample. The signatures of the $CH_2$ and $CH_3$ chemical groups are hardly seen at around 3400 nm, due to the low signal-to-noise ratio. A dramatic decrease of intensity of the water band is observed in the case of the 40 GPa sample, in agreement with transmission infrared measurements on the matrix grains.

The Raman spectra were collected with a 514 nm excitation laser on raw matrix grains (Fig. 4). The spectra show the first-order carbon G and D bands, centered at ~1580 and ~1350 cm$^{-1}$, respectively. We visually observed a drop in the intensity of the fluorescence background with increasing peak pressure (Fig. 4). No spectral variations in the G and D bands can be observed with the naked eye, showing that IOM did not experience a large reorganization of its carbon skeleton. Nevertheless, the LBWF fit of the G and D bands reveals significant variations in the Raman parameters (Fig. 5, Table 3). In the FWHM-G vs. $\omega_G$ diagram, the samples shocked at ≤20 GPa form a fairly well defined trend, with no correlation between points position and peak pressure. Samples shocked at 40 and 50 GPa plot below this subgroup, and 50 GPa samples even display lower FWHM-G and higher $\omega_G$ parameters with respect to the other samples (Fig. 5, top-right). In the FWHM-D vs. $I_D/I_G$ diagram, we still observe a grouping of 0–20 GPa shocked samples, and detached 40 and 50 GPa samples that display a lower $I_D/I_G$ ratio.

### 3.2. Analyses on Murchison IOM

Similar behaviors can be seen in the Raman measurements collected on purified IOM, but the IOM data points of each sample are more tightly clustered. For instance, the FWHM-D parameters of the 0–20 GPa IOM samples are very similar (except maybe the first session of 20 GPa experiments; Fig. 5), but in contrast FWHM-D values determined from raw matrix samples are more scattered. In order to check the consistency of both sets of measurements, the different parameters for IOM and raw matrix measurements were plotted against each other (Fig. 6). $\omega_G$, FWHM-G and $I_D/I_G$ show good correlations between bulk and IOM data. The correlation is slightly worse in the case of FWHM-D, and a lack of correlation is observed for $\omega_D$. The larger data dispersion observed in

**Table 3**
Raman parameters.

| Sample | P-Peak (GPa) | FWHM-G ($cm^{-1}$) | $\omega_G$ ($cm^{-1}$) | FWHM-D ($cm^{-1}$) | $\omega_D$ ($cm^{-1}$) | $I_D/I_G$ |
|---|---|---|---|---|---|---|
| Murchison | 5 | 102 ± 4 | 1590 ± 3 | 223 ± 10 | 1362 ± 3 | 0.89 ± 0.05 |
| (Bulk) | 10 | 99 ± 5 | 1592 ± 3 | 211 ± 12 | 1361 ± 4 | 0.91 ± 0.03 |
| | 20 | 101 ± 6 | 1591 ± 4 | 207 ± 12 | 1363 ± 3 | 0.91 ± 0.03 |
| | 20 | 104 ± 5 | 1587 ± 3 | 230 ± 9 | 1367 ± 4 | 0.88 ± 0.04 |
| | 40 | 98 ± 6 | 1588 ± 3 | 235 ± 16 | 1366 ± 5 | 0.76 ± 0.04 |
| Murchison | 0 | 94 ± 4 | 1593 ± 1 | 206 ± 5 | 1362 ± 2 | 0.85 ± 0.03 |
| (IOM) | 5 | 93 ± 3 | 1594 ± 1 | 208 ± 5 | 1364 ± 2 | 0.86 ± 0.02 |
| | 10 | 94 ± 3 | 1594 ± 1 | 204 ± 6 | 1364 ± 2 | 0.86 ± 0.03 |
| | 20 | 99 ± 4 | 1591 ± 2 | 213 ± 6 | 1367 ± 3 | 0.84 ± 0.04 |
| | 20 | 95 ± 6 | 1593 ± 2 | 208 ± 8 | 1365 ± 3 | 0.86 ± 0.03 |
| | 40 | 88 ± 5 | 1592 ± 2 | 213 ± 5 | 1364 ± 2 | 0.74 ± 0.02 |
| | 50 | 80 ± 6 | 1595 ± 2 | 202 ± 15 | 1358 ± 4 | 0.74 ± 0.02 |
| EET 90628 | 0 | 66 ± 21 | 1601 ± 4 | 212 ± 14 | 1354 ± 5 | 0.72 ± 0.04 |
| (Bulk) | 5 | 70 ± 6 | 1603 ± 3 | 197 ± 13 | 1352 ± 4 | 0.76 ± 0.06 |
| | 10 | 72 ± 6 | 1602 ± 2 | 197 ± 20 | 1355 ± 5 | 0.77 ± 0.05 |
| | 20 | 80 ± 11 | 1597 ± 6 | 205 ± 13 | 1352 ± 4 | 0.82 ± 0.08 |
| | 30 | 86 ± 8 | 1596 ± 4 | 192 ± 22 | 1353 ± 2 | 0.86 ± 0.04 |
| | 40 | 82 ± 9 | 1598 ± 4 | 193 ± 17 | 1353 ± 3 | 0.82 ± 0.05 |
| | 50 | 79 ± 7 | 1599 ± 3 | 193 ± 14 | 1351 ± 3 | 0.85 ± 0.05 |

Data given with ±1 standard deviation.

raw matrix data is, at least partly, due to uncertainties in the baseline removal. Indeed, a visual inspection of the whole data set reveals that the raw matrix spectra display a higher fluorescence and a lower intensity of the G and D bands, compared to the IOM data. This has the largest impact on the width and position of the D band during baseline subtraction, because the LBWF fit with a constant set to zero cannot fit accurately the D band wing at low wavenumbers. Finally, these cross-measurements show that the CsF/HCl acid digestion procedure employed for extracting IOM does not modify significantly the poly-aromatic structure. This is an interesting finding, as this point is regularly questioned.

The infrared spectra of Murchison IOM are shown in Fig. 7. The blue spectrum corresponds to IOM extracted from an unshocked sample of Murchison, which can be conveniently described using four regions of interest: (1) 3600–3000 $cm^{-1}$: this broad feature is controlled by the stretching mode of OH groups in alcohols or carboxyls. This band may be blurred by continuum and baseline subtraction if the baseline is modulated by interference fringes. (2) 2800–3000 $cm^{-1}$: this region displays four peaks, but is a complex congested structure involving the symmetric and anti-symmetric stretching modes of CH, $CH_2$ and $CH_3$ groups, as well as overtones and Fermi resonance interactions (MacPhail et al., 1984). Practically speaking, only five components are distinguishable and used for semi-quantitative estimation of the $CH_2/CH_3$ ratio, while the integrated absorbance of the whole band provides an estimate of the aliphatic abundance. (3) 1800–900 $cm^{-1}$: this region contains a band at ~1700 $cm^{-1}$ due to carbonyl groups, a band at ~1600 $cm^{-1}$ due to the C=C bond in aromatic rings, and a broad, spectrally congested structure extending from 1500 $cm^{-1}$ to 900 $cm^{-1}$, which includes several vibrations modes, i.e., bending and deformation modes of $CH_2$ and $CH_3$, the stretching mode of C-O bond, etc. (Kebukawa et al., 2011; Orthous-Daunay et al., 2013; Painter et al., 1981).

At 5 GPa, the spectrum is very similar to that of unshocked Murchison, except for the appearance of a faint feature at 1653 $cm^{-1}$, and a slightly higher intensity of the $CH_2$ versus $CH_3$ antisymmetric stretching modes in the 2800–3000 $cm^{-1}$ feature (Table 4). At 10 GPa, we observe an increased intensity of these two features, with a feature at 1656 $cm^{-1}$. Spectra collected for the two 20 GPa sessions reveal significant differences. In the first session, the new feature is hardly seen, and the 2800–3000 $cm^{-1}$ aliphatic band is very noisy and not suitable for semi-quantitative analysis. We note as well a decrease of the carbonyl band at 1710 $cm^{-1}$. For the second session, the new feature is intense and located at 1651 $cm^{-1}$. At 40 GPa, an intense feature is centered at 1656 $cm^{-1}$, the carbonyl band is weak and we observe a dramatic increase of the intensity of the $CH_2$ antisymmetric stretching mode versus that of $CH_3$. Last, at 50 GPa, the two samples display spectra that are similar to that of the 40 GPa samples, and one of them displays a narrow band at 1730 $cm^{-1}$, showing substantial heterogeneity. Overall, the aliphatic band is weak. The feature at ~1650 $cm^{-1}$ band is possibly present in the spectra of coal, which are very congested in the spectral range 1600–2000 $cm^{-1}$. Several components involving N–H and/or quinone groups have been proposed (Painter et al., 1981). The attribution to N–H is unlikely, due to the low abundance of nitrogen and the lack of N–H stretching modes in the 3000 $cm^{-1}$ region. Quinones display a band in the range 1650–1670 $cm^{-1}$, depending on the number of rings and substitutions (Ibarra et al., 1996; Lin-Vien, 1991; Petersen et al., 2008). More generally, highly conjugated carbonyl displays a stretching vibration band around 1650 $cm^{-1}$.

The infrared spectra were processed using the following procedure. The C=C band at 1600 $cm^{-1}$ was normalized to 1. The carbonyl abundance was measured as the peak intensity of the C=O band at ~1700 $cm^{-1}$ ($I_{C=O}$). The aliphatic abundance was estimated by the integrated absorbance of the aliphatic band in the range of 2700–3000 $cm^{-1}$ ($A_{ali}$). The ratio of the abundances of the $CH_3$ and $CH_2$ groups was estimated by calculating the intensity ratio of the antisymmetric stretching modes of these groups ($I[CH_2]/I[CH_3]$). It is important to emphasize that these parameters are all only semi-quantitative. Fig. 8 shows that the aliphatic abundance decreases significantly at 40 GPa and 50 GPa. No monotonic trend is observed between 5 GPa and 40 GPa, and at 10 GPa we even observe a value that is higher than that of the unshocked material. The $I[CH_2]/I[CH_3]$) ratio increases after shock for all samples, but no clear trend is observed with the peak pressure. The carbonyl abundance decreases in all shocked samples. Note that we have ignored the 50 GPa samples with the narrow C=O band at 1730 $cm^{-1}$ that was produced by the shock.

The carbon-XANES spectra of IOM from the experimentally shocked Murchison meteorite samples are shown in Fig. 9 (see a C-XANES spectrum of unshocked Murchison). All the spectra exhibit peaks of aromatic/unsaturated carbon (C=C*) at 285.2–285.6 eV (peak B);

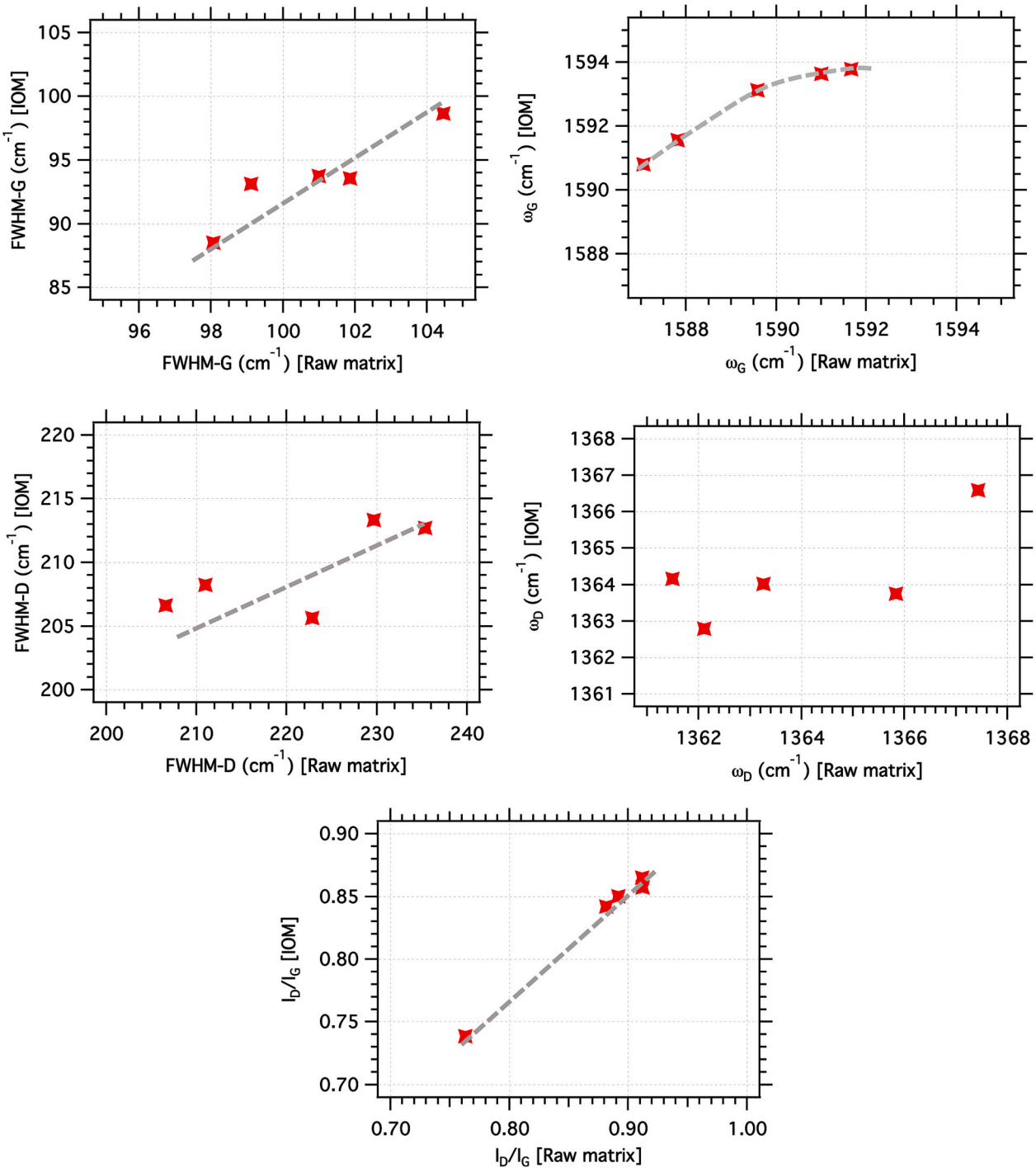


**Fig. 6.** Comparison or Raman parameters derived from spectra collected on IOM (y-axis) and bulk samples (x-axis). A good correlation is observed for all these parameters, except for $\omega_D$. For this parameter, the discrepancy is due to the baseline subtraction, which is perturbed by the high fluorescence signal in the Raman spectra collected on bulk samples. As a conclusion, the HF/HCl digestion technique has negligible effects on the polyaromatic structure.

aliphatic carbon (C*Hx) (peak C) at 287.3–288.1 eV and carboxyl carbon (C*OOH) (peak D) at 288.4–288.7 eV. The spectra of the 5–20 GPa IOM are very similar to that of unshocked Murchison IOM (Cody et al. 2011, see their Fig. 5), except for the absence of the peak derived from aromatic ketone at 286.5 eV. At 20 GPa, the peak intensity of carboxyl carbon is slightly higher than those at 5 and 10 GPa. At 40 and 50 GPa, the peak intensities of carboxyl carbon are remarkably lower than those at 5–20 GPa. On the other hand, the peak intensities of aromatic carbon in the 40–50 GPa IOM are slightly high and broad compared to those at lower pressures. In addition, small shoulders at 283.7–284 eV, which are likely assigned to quinone, newly appeared in the 40–50 GPa IOM. The 1s-σ* exciton (291.6 eV) peak of highly conjugated $sp^2$ carbon was not seen in any spectra, while the broad spectral feature ranging from 292 to 296 eV due to the 1s-σ* transition of aromatic C*=C moderately developed in the 50 GPa.

The NanoSIMS isotope analyses on extracted IOM are shown in Fig. 10aa and 10b, and averages calculated from images are tabulated in Table 5. The bulk δD for the unshocked Murchison is 1636 ± 529 ‰. Two IOM grains of unshocked Murchison show significant δD spatial variations, with several isotopic hot spots. A third grain shows lower δD

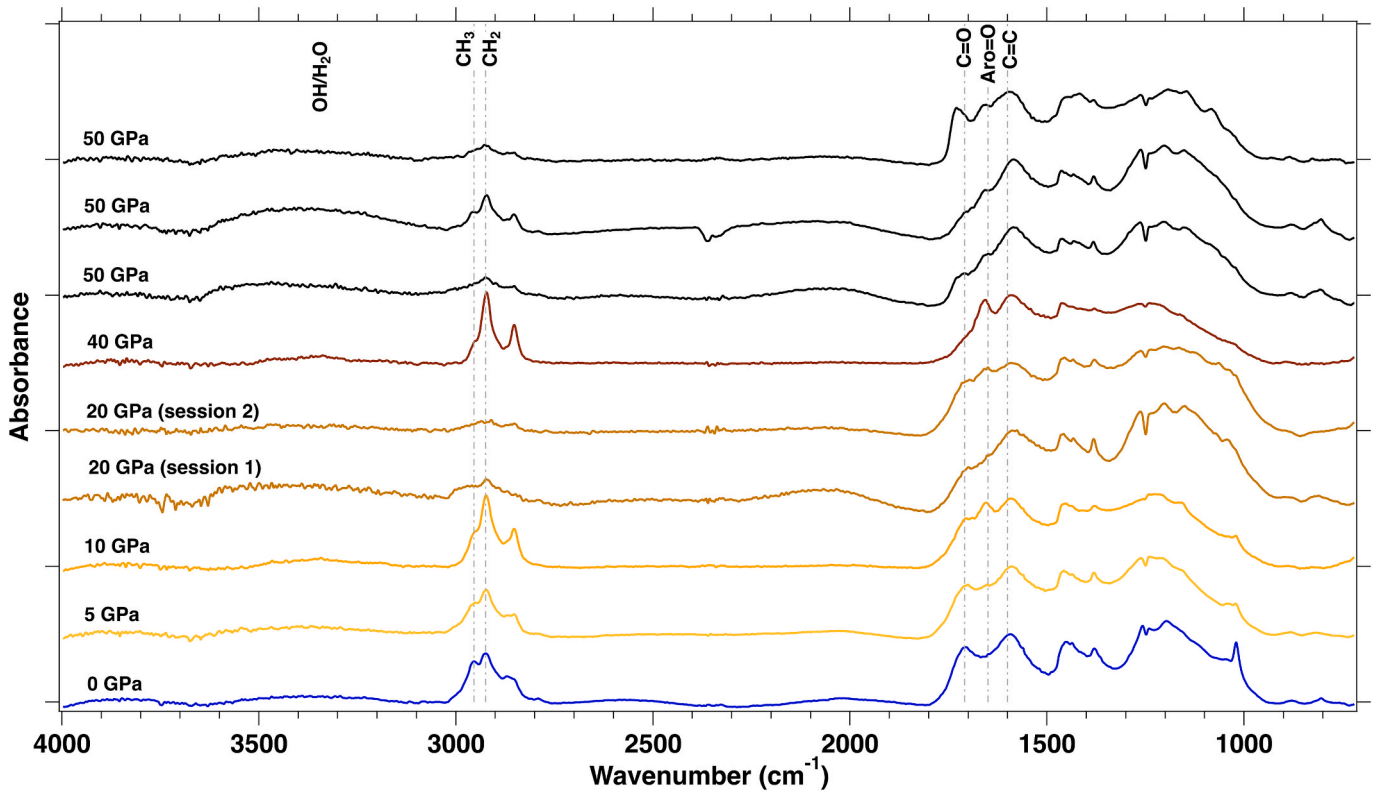


**Fig. 7.** Infrared spectra (baseline corrected) of the Murchison IOM samples extracted from the shocked samples.

**Table 4**
IR parameters.

| Sample | P-Peak (GPa) | $I_{CH2}/I_{CH3}$ | Abs. Int. Aliphatic | I-1657 | I-1700 |
|---|---|---|---|---|---|
| Murchison (IOM) | 0 | 1.2 | 72.4 | – | 0.81 |
| | 5 | 1.4 | 59.7 | 0.73 | 0.73 |
| | 10 | 2.0 | 79.0 | 0.94 | 0.70 |
| | 20 | 3.2 | 61.4 | 0.92 | 0.42 |
| | 40 | 2.1 | 28.9 | 0.92 | 0.23 |
| | 50 | 1.9 | 36.7 | 0.55–0.80 | 0.35 |

values across the image and less hot spots. This heterogeneity results in a high standard deviation. At 5 GPa, the bulk δD value drops dramatically and only a few hot spots remain (297 ± 147 ‰). For samples shocked at 10 GPa and 20 GPa, we observe a slight increase of the bulk δD with respect to 5 GPa (297 ± 147 ‰, 465 ± 70 ‰ and 650 ± 220 ‰). Finally, at 40 GPa, the three analyzed grains no longer show any hot spots and appear relatively homogeneous, with a negative bulk δD (−79 ± 18 ‰).

### 3.3. Shock experiments on EET 90628

The Raman parameters collected on EET 90628 at 0, 5, 10, 20, 30, 40 and 50 GPa are displayed on Fig. 11. We observe overall an almost monotonic decrease of FWHM-D and an increase of $I_D/I_G$. The 50 GPa sample then plots close to the ordinary chondrite Bishunpur (LL/3.1). However, the G band parameters in the range 20–50 GPa do not fit with those of type 3 chondrites. We observe overall a decrease of $\omega_G$ and an increase of FWHM-G (Fig. 11). These trends are strikingly different than those observed for shocked Murchison, for which we observe a drop of $I_D/I_G$, $\omega_G$ and FWHM-G, and a moderate decrease of FWHM-D. No IOM was extracted from the shocked EET 90628 samples.

## 4. Discussion

### 4.1. Carbonization process

Insoluble Organic Matter experienced compositional and structural transformations during the shock experiments, which point to a carbonization process. The peak ratios of the $CH_2$ and $CH_3$ antisymmetric stretching modes in FTIR spectra increases from 5 to 20 GPa, and then drop for 40 and 50 GPa. The integrated absorbance of the aliphatic bands (2800–3000 $cm^{-1}$) is lower in the shocked samples, except at 10 GPa. The peak intensity of the carbonyl peak at 1700 $cm^{-1}$ decreases with increasing the shock stage (Fig. 8), which is consistent with the decrease of carboxyl group in the C-XANES spectra at 40 and 50 GPa (Fig. 9). In addition, the broader peaks of aromatic carbon in the C-XANES spectra at 40 and 50 GPa are probably reflected by the increase of the number of aromatic rings. All these trends indicate the loss of hydrogen and aliphatic functional groups, decarbonylation (decarboxylation), and, likely, the formation of aromatic carbon. The presence of a presumably quinone group at higher pressures, observed both in FTIR and C-XANES spectra, is intriguing, as it is not observed in unshocked chondritic IOM. The appearance of this functional group suggests that an oxidation process operated during the shock. The chemical heterogeneity (Fig. 7) that is observed at the μm spatial scale reflects the heterogeneity of the shock heating within the samples, which is consistent with the local melting observed in shocked Murchison by Tomeoka et al. (1999). The structural evolution of IOM observed in the Raman spectra is, however, very limited. In the range 0–20 GPa, the shocked samples are not clearly distinguishable from the starting Murchison IOM. Significant effects are observed at 40 and 50 GPa: the decrease of $I_D/I_G$ and FWHM-G, while FWHM-D is constant until 40 GPa, followed by a small drop at 50 GPa. They are however very limited, with no substantial formation of highly conjugated aromatic units, which is also consistent with the absence of the 1s-σ* exciton in C-XANES spectra at 40 and 50 GPa. Note that the raw spectrum for 20 GPa shows a lower fluorescence

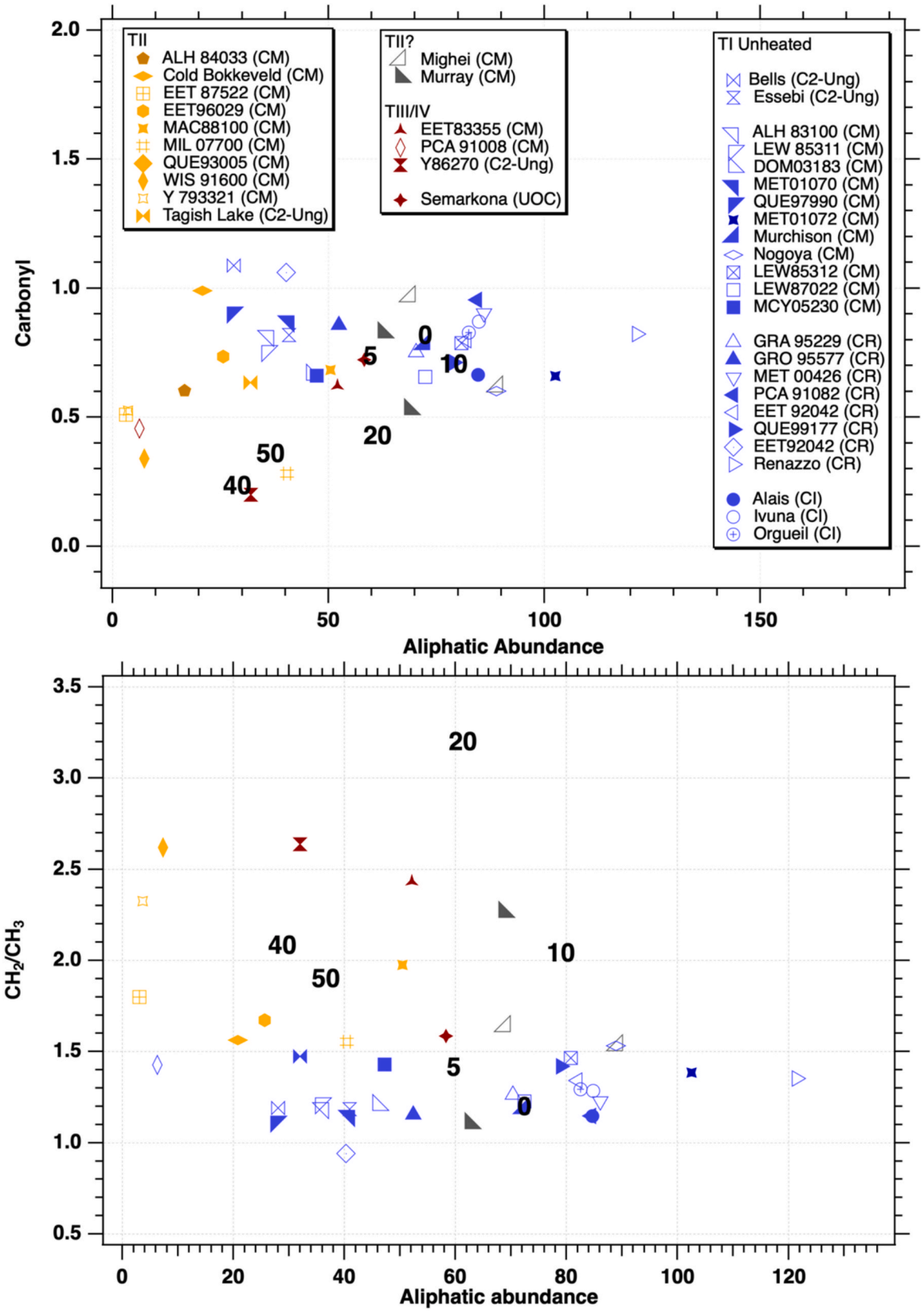


**Fig. 8.** The infrared parameters extracted from the infrared spectra shown in Fig. 6, plotted together with those of series of TI, TII and TIII/IV chondrites. (data from Quirico et al., 2018).

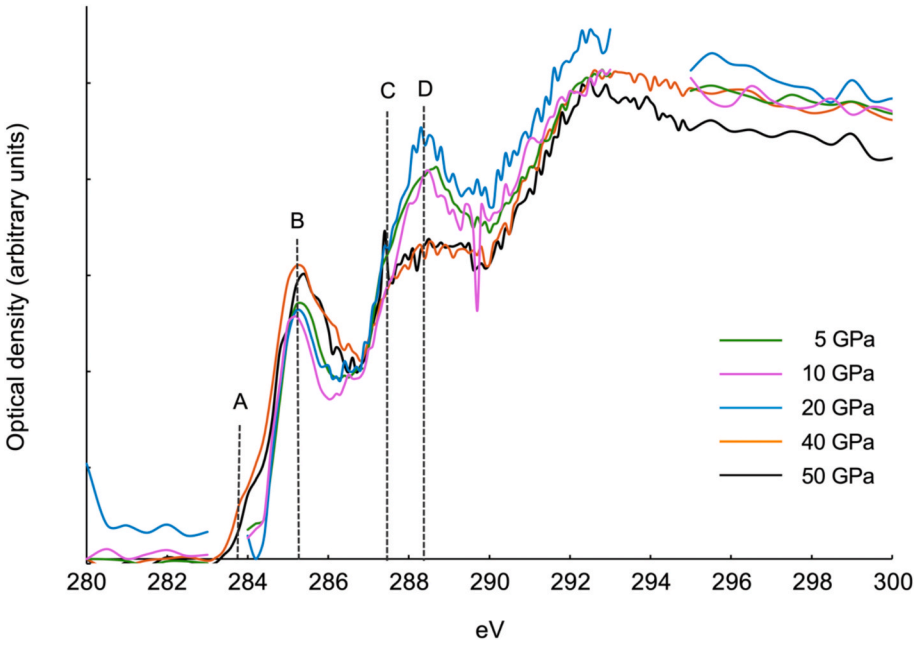


**Fig. 9.** Carbon XANES spectra of the IOM extracted from the Murchison meteorite samples shocked at 5, 10, 20, 40, and 50 GPa. Peak assignments are based on Cody et al. (2008). Peak A: Quinone (C=C*-C=O) at 283.7 eV. Peak B: 1s-π* transition for aromatic carbon (C=C*) at 285.2–285.6 eV. Peak C: 1s-3p/s* transition for aliphatic carbon at CHx-C at 287.3–288.1 eV. Peak D: 1s-π* transition for carbonyl carbon in carboxyl or ester (OR(C*=O)C) at 288.4–288.7 eV.

background, but no substantial difference is provided by parameters of the fit of the data.

Shock or post-shock temperatures have been determined for CV (Nakamura, 2000), CM (Hu and Sharp, 2022), and ordinary chondrites (Schmitt et al., 1994). These calculations hold for a single-shock process and the derived temperatures are upper limits. Indeed, the peak experimental shock pressure is achieved through multiple reverberations and the released energy is generated by the first propagation, before reflection. All these calculations indicate that porosity is an important parameter in determining the peak temperature. For Allende, which is modeled as an olivine dominated-material with 20 % of porosity, calculations give peak temperatures of ~700 °C at 20 GPa and ~ 1300 °C at 40 GPa (Nakamura, 2000). For a L chondrite with a porosity of 11 %, a peak temperature of 1200 °C is obtained for a pressure of 50 GPa (Schmitt et al., 1994). For a CM (Murchison) chondrite, peak temperatures of 215, 480, 1067, 2434 and 3208 °C, are estimated for shock pressures of 5, 10, 20, 40 and 50 GPa, respectively (Hu and Sharp, 2022). Our own calculations based on the determination of waste heat energy are consistent with Hu and Sharp (2022) and show an overestimation of the shock and post-shock temperatures (Table 2). As mentioned in section 2.2, the measurements of Tomioka et al. (2007) corrected with $C_v$ = 800 kJ.kg$^{-1}$.K$^{-1}$ could be more realistic, as they have used a more sophisticated numerical modeling based on the Autodyn 2D code. These values, as 63 °C at 10 GPa; 370 °C at 21 GPa; 638 °C at 36 GPa; 1104 °C at 49 GPa, appear finally quite close to the estimates of Nakamura et al. (2000). Nevertheless, it is clear that more thorough modeling, and new experimental data about the thermodynamic properties and EOS of chondritic materials, are needed in the future to propose robust estimates.

Anyhow, with these estimates in hand, it is interesting to compare the shocked samples with heating experiments conducted on primitive carbonaceous chondrites. Chan et al., (2019) report Raman measurements on Tagish Lake samples heated at 600 °C and 900 °C for durations of 1 h and 96 h at each temperature. Upon heating, FWHM-D decreases and $I_D/I_G$ slightly increases. To first order, $\omega_D$ and $\omega_G$ decreases and increases, respectively, for the 600 °C and 900 °C groups of data. In detail, the data points at 600 °C (for 1 h and 96 h durations) are the opposite of the global trend. No monotonic variations of FWHM-G with the degree of heating is observed. It is noteworthy that these Raman data are not strictly comparable to the data presented here. First, the Tagish Lake lithologies that were used in this study are likely assigned TII (to our knowledge, the i11 lithology is thermally processed in the parent body, and its IOM is slightly more ordered than that of a TI chondrite such as Murchison) (Quirico et al., 2018). Second, the photon density was higher by a factor ~ x4, and the Lorentzian + Breit-Wigner-Fano fit model was run using a floating baseline (see their Fig. S2), leading to drifts in the parameters. Despite these potential drawbacks and the low number of samples, they are consistent with the evolution of Raman parameters in type 3 chondrites, in particular the lack of correlation between FWHM-G and the peak temperature, and the increase of $I_D/I_G$ (see Bonal et al., 2016). Interestingly, the degree of structural order achieved in the samples heated by Chan et al. (2019) is much higher than that in Murchison samples shocked at 40 GPa and 50 GPa. A weak drop is observed at 50 GPa, while FWHM-D decreases from ~ 300 cm$^{-1}$ to ~ 200 cm$^{-1}$ in heating experiments at 900 °C. In addition, no decrease of $I_D/I_G$ is observed in the very first stages of these heating experiments, but this may be due to the different parent body heating experienced by the two meteorites (TI and TII). Flash-heating experiments on bulk Murchison powders reported in Muirhead et al. (2012) also show an increase of the $I_D/I_G$ parameter with increasing temperature (plateau in the range 250–1000 °C; duration of 5–80 s; but no information on the heating rate) (see their Fig. 1a). This publication does not report values for the D-band width, but naked-eye observations suggest that there is no dramatic decrease in this parameter, and then no substantial evolution of the structural order. Riebe et al. (2020) report flash-heating experiments on the IOM extracted from the chondrite Cold Bokkeveld, at 400, 600, 800 and 1000 °C during 4 s. They show that FWHM-G and $\omega_G$ decreases and increases, respectively, upon the heating temperature. No significant evolution of FWHM-D is reported, showing the lack of any substantial structural evolution of the IOM. Note that Cold Bokkeveld is a type TII chondrites.

The kinetics, peak temperature, and heating rate conditions are very different between all these experiments. At 900–1000 °C, it is quite clear that heating times of tens of seconds versus 1 h lead to dramatic differences in terms of structural order, while much less significant transformations are observed between 1 and 96 h. This is because kinetic

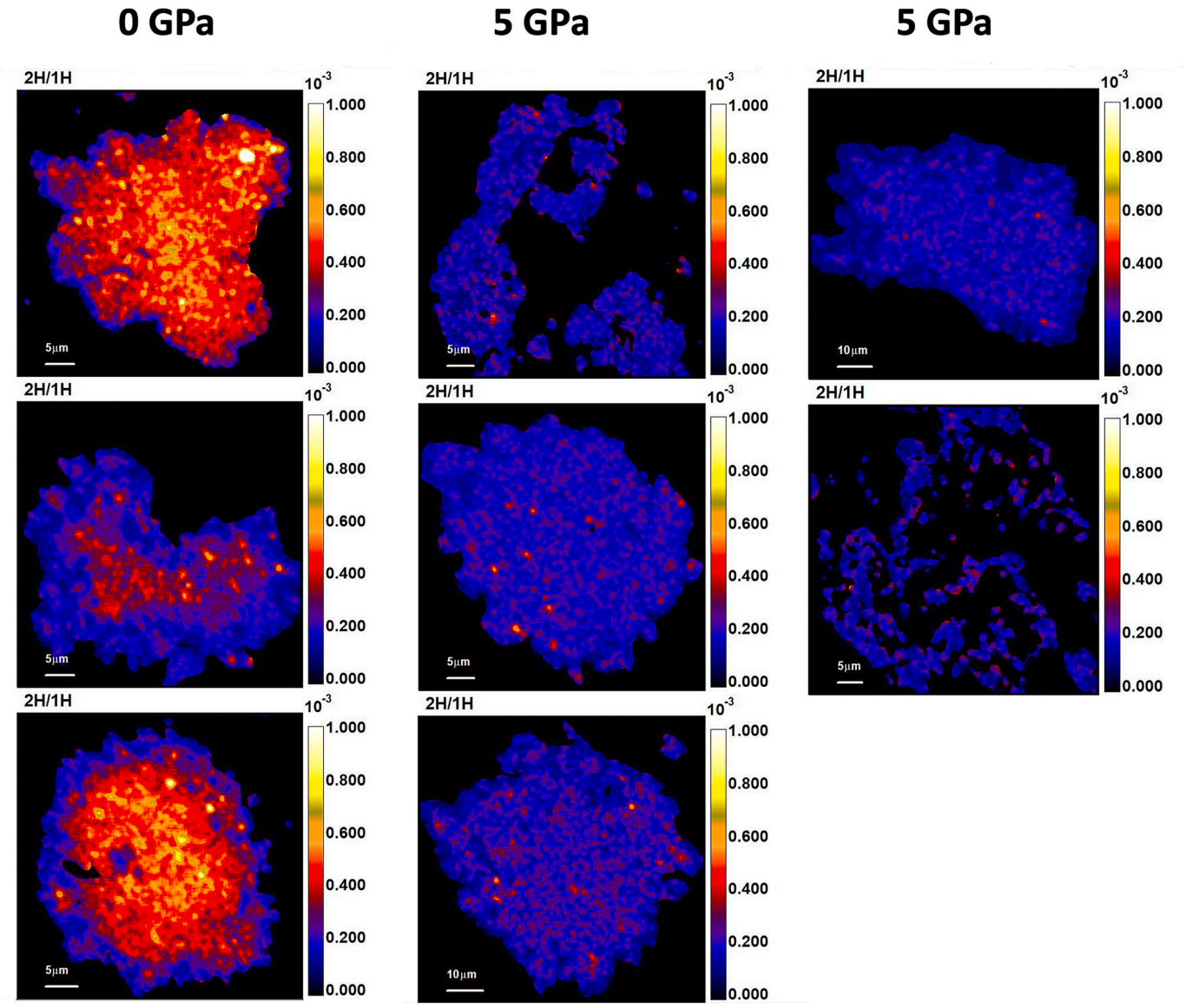


**Fig. 10a.** D/H maps in IOM recovered from Murchison samples before shock experiments and after shock experiments at 5 and 10 GPa.

behavior is linear in time but follows an exponential dependence with the temperature. The differences between flash or short-duration pyrolysis (~ms-s) and shock recovery experiments may also be due to kinetics. In shock recovery experiments, the typical duration of the pressure peak is ~ µs (Miyahara et al., 2021), which is at least 3 orders of magnitude lower, while the recalculated shock temperatures of Tomioka et al. (2007) (Table 2) are in the range of those used in the above-mentioned flash heating studies.

In many studies, especially those aimed at char production for industrial purposes, the heating rate appears as a key parameter controlling carbonization (Kaneki and Hirono, 2018; Lievens et al., 2013; Nachenius et al., 2013). This is due to the fact that carbonization is an irreversible process involving a complex sequence of many reactions with their own kinetics (pre-exponential factor and activation energy Ea). It can also be related to the confinement and diffusion kinetics of carbonization by-products, which undergo secondary carbonization. Thermal degradation experiments of biomass, coals and simple biopolymers (lignin, cellulose) show that carbonized solids (chars) are usually obtained at low temperatures with low heating rates, while flash pyrolysis with high heating rates (up to 1000 °C/min) and short reaction times (<2 s) favors liquid and gas production. In the case of chondrites, however, the highly cross-linked macromolecular structure of IOM prevents from the production of liquid and releases only 30–50 wt% volatiles in flash heating experiments (Okumura and Mimura, 2011; Riebe et al., 2020). The heating rate in a shock experiment varies between ~ $4 \times 10^7$ to $1 \times 10^9$ K·s$^{-1}$, using the recalculated shock temperature estimates of Tomioka et al. (2007). These values are much higher than those obtained in flash heating experiments with pyrolyzers ~ $10^2$–$10^3$ K·s$^{-1}$, which is less favorable to the formation of aromatic species.

Another physical parameter that may control carbonization is confinement and pressure. In this case, the migration of by-products is reduced, promoting secondary carbonization. Frictional heating experiments show efficient carbonization of low rank coals due to the mechanical effect of shear stress (Furuichi et al., 2015; Kaneki et al., 2018; Kaneki and Hirono, 2018). Nevertheless, in the experiments of Kaneki et al. (2018), $I_D/I_G$ increases upon heating, as observed in heating experiments performed at normal pressure or in vacuum. These friction experiments cannot be directly extrapolated to shock conditions. Finally, the main conclusion that emerges is that the duration of heating is the main parameter that accounts for the differences between IOM carbonization observed in shock experiments and heating experiments

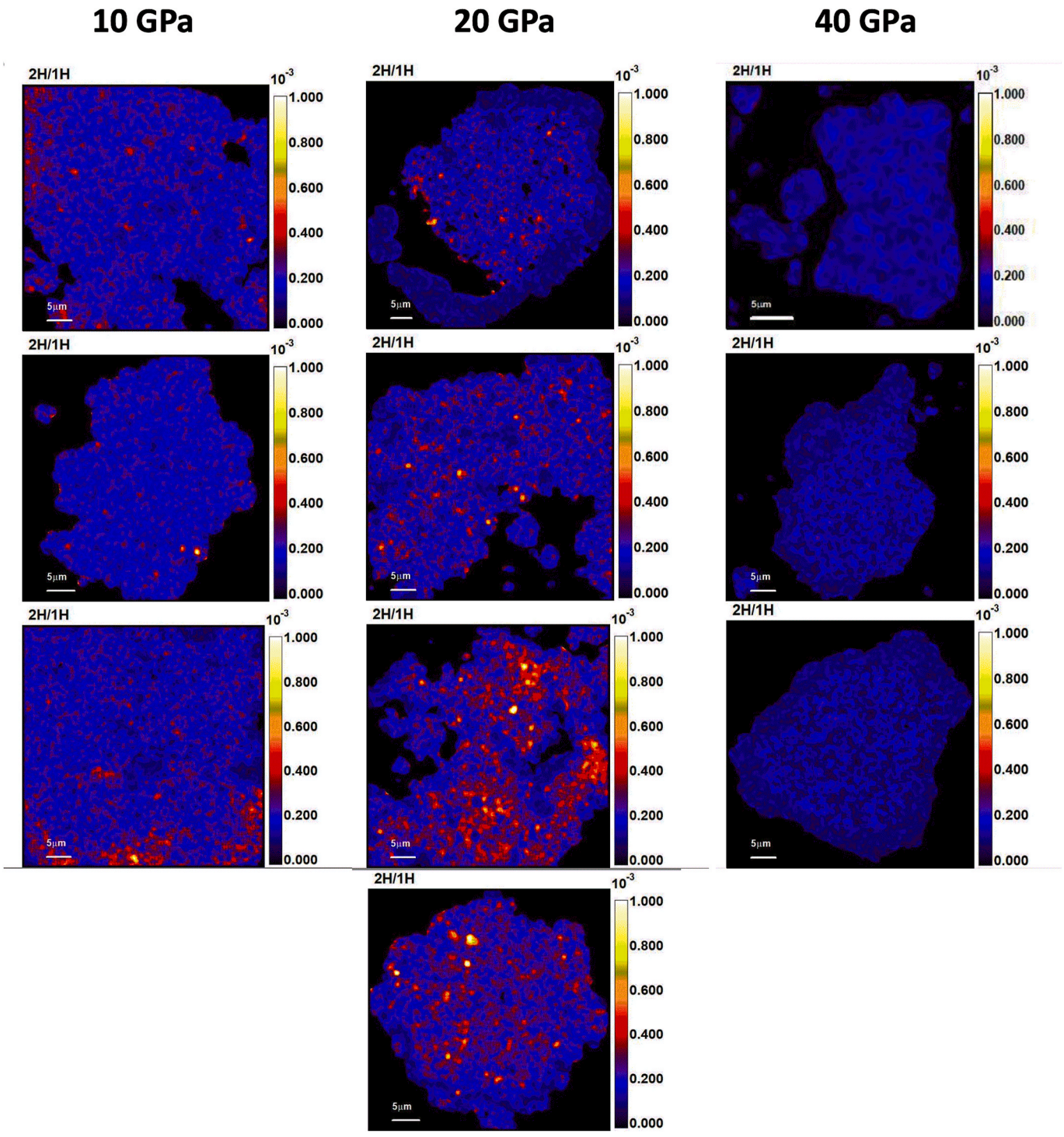


**Fig. 10b.** D/H maps in IOM recovered from Murchison samples shocked at 20 GPa and 40 Pa.

over hours.

Experiments on the ordinary chondrite EET 90628 show different evolutionary trends compared to Murchison. In the case of EET 90628, $I_D/I_G$ increases while FWHM-D decreases with an increasing peak pressure, consistent with heating experiments performed on terrestrial organic matter and Type 3 chondrites. In contrast, in the case of Murchison, no clear trend was observed for FWHM-D, while $I_D/I_G$ decreased for 40 and 50 GPa. The trends for EET 90628 are consistent with observations of thermally metamorphosed Type 3 chondrites, in the range of petrologic type 3.0–3.1 (Fig. 11). EET 90628 is classified as L3.0, but as mentioned above the petrological subtype is ambiguous because this chondrite has experienced a mild degree of thermal metamorphism and was more heated than Murchison in its parent body. Consistent with this, the IOM in EET 90628 is different from that of Murchison and has a higher degree of $sp^2$ organization (i.e., larger size of the polyaromatic units) (Bonal et al., 2016; see Fig. 3). In this respect, the starting points of the samples in the shock experiments were not the same, and one explanation for the differences in the response of the IOM from the two meteorites to shock heating is that the very first stage of carbonization observed in the case of Murchison had already occurred in the parent body of EET 90628. Another explanation is that the mineralogical environment of IOM show substantial differences in these two

**Table 5**
The δD composition of extracted IOM from Murchison and shocked Murchison at 5, 10, 20 and 40 GPa. The second column shows bulk values for individual fragments for each sample, while the third column shows the average of the fragment values.

| Peak Pressure (GPa) | δD (‰) ROIs | δD (‰) Bulk |
|---|---|---|
| 0 | 2095 | 1640 ± 530 |
| | 1058 | |
| | 1756 | |
| 5 | 223 | 296 ± 147 |
| | 410 | |
| | 476 | |
| | 256 | |
| | 113 | |
| 10 | 532 | 465 ± 66 |
| | 400 | |
| | 462 | |
| 20 | 424 | 648 ± 222 |
| | 493 | |
| | 868 | |
| | 809 | |
| 40 | −63 | −79 ± 18 |
| | −76 | |
| | −98 | |

chondrites. The matrix modal abundance in Murchison is about 60 vol%, and ~ 23 vol% in EET 90628 (Eschrig, 2022). More critically, the matrix of EET 90628 is poorly hydrated compared to Murchison, 7.8 wt% and 1.75 wt%, respectively (Garenne et al., 2014; Eschrig, 2022), and less extensive interactions between organic matter and water or hydroxyl groups are expected. These interactions also happened in the shock experiments, but it is unknown whether the final by-products are the same than those produced by a slow radiogenic heating.

An interesting potential implication of these results is the role of shock effects superimposed on radiogenic thermal metamorphism in the case of Type 3 chondrites. As mentioned above, there is no clear correlation between FWHM-G, $\omega_G$ and the petrological subtype (Bonal et al., 2016). This major difference with the case of terrestrial organic material, either heated in the laboratory or carbonized for long periods in sedimentary basins (~Ma), could be explained by two competing carbonization processes (shock and radiogenic).

### 4.2. C2 heated chondrites vs. shocked samples in the laboratory

A major issue is the representativeness of shock experiments for reproducing the composition and structure of the IOM, the mineralogical compositions and the textures of the assemblages in type 1 and 2 carbonaceous chondrites. Our results show that shocked Murchison samples undergo progressive dehydration (Fig. 2). The OH band at 3670 $cm^{-1}$ in the infrared spectra of the matrix samples shows that serpentines are present up to 20 GPa and are completely decomposed at 40 GPa, but molecular water is still present. The broadening of the 1000 $cm^{-1}$ SiO band indicates the progressive structural modification of phyllosilicates and the formation of amorphous silicates, presumably formed from vein melts coexisting with the host matrix. At 40 GPa, the spectra also indicate the presence of olivine. The shock-recovery experiments of Tomeoka et al. (1999), conducted on Murchison chips, reveal significant modifications of the texture and of the nature of minerals at pressures ≥ 20 GPa. Matrix melting was found to occur in the range 20–30 GPa, and to be very heterogeneous and localized in fractures, presumably because it is controlled by frictional heating and enhanced by porosity. Between 30 GPa and 35 GPa, vesicular melts formed pervasively throughout the matrix, driving serpentines dehydration and, to a lesser extent, carbonate decomposition. Tyburczy et al. (1986) report an early dehydration in Murchison samples at 11 GPa, but did not run experiments below this peak shock pressure. The decomposition of terrestrial Mg-rich serpentines, as antigorite, lizardite and chrysotile, starts at 600 °C (Weber and Greer, 1965). However, thermogravimetric analyses run on a series of carbonaceous chondrites support a range of decomposition temperatures of 400–770 °C, which reflects the broad range of serpentine Fe/Mg ratios, and the low crystallinity of serpentines in CM chondrites (Beck et al., 2010; Garenne et al., 2014). With those data in hand, the results of Tomeoka et al., (1999) point to localized temperatures above 400 °C in the range 20–30 GPa, which extend to the whole sample at 40 GPa and above. Overall, our results are consistent with these observations.

Fig. 13 shows bulk infrared spectra of heated C2 chondrites (pellets made of ground meteorites), along with matrix grains of Murchison shocked at 5 and 40 GPa. Though bulk infrared spectra include the spectroscopic features of chondrules, this contribution mostly appears as a weak peak at 890 $cm^{-1}$ and the comparison between the two set of data is suitable for our purpose. At 40 GPa, the infrared spectrum is consistent with a TIII heating grade, i.e. a mix of amorphous materials and neoformed olivines. The spectra of Pecora Escarpment (PCA) 91008 and EET 83355, both assigned a TIII according to Tonui et al. (2014), show different degrees of recrystallization of amorphous materials: PCA 91008 is more thermally processed than EET 83355. The sample shocked at 40 GPa seems to lie between TII chondrites (e.g., WIS 91600, MIL 07700) and EET 83355. Our experiments did not provide petrographic information. However, according to Tomeoka et al. (1999), above 30 GPa, chondrules and matrix are heavily disrupted. This observation is at odds with petrological observations of several TIII/IV heated chondrites, where well rounded chondrules are observed, e.g. PCA 91008, PCA 02012, Yamato (Y-) 86720, EET 83355 (Tonui et al., 2014; and see as well petrographic descriptions in the Meteoritical Bulletin Database). Therefore, the shock intensity experienced by natural samples was lower than 30 GPa, and in that case the shock recovery experiments cannot reproduce the mineralogy of TIII/IV heated chondrites (i.e., mixtures of amorphous materials and olivines or pyroxenes).

Regarding IOM, the Raman parameters measured on samples shocked below 20 GPa plot with unheated chondrites (Fig. 12). The sample shocked at 40 GPa display $I_D/I_G$ values consistent with TII chondrites but not with TIII/IV chondrites, and their FWHM-D values remain higher than 200 $cm^{-1}$, while TIII/IV chondrites plot below this (dotted circles in Fig. 12). In this respect, short-duration heating in C2 chondrites is better simulated with heating at 1 bar or under vacuum for 1–96 h (e.g., Chan et al. 2019; Nakato et al. 2008). Another striking difference between the shock experiments and natural samples is that in the shock experiments we first observe a progressive chemical evolution of the IOM (e.g., the increase of the $n[CH_2]/n[CH_3]$ ratio and the loss of carbonyl groups) and then a structural evolution. Even at 5 GPa, we observe in the infrared spectra a slight increase of $CH_2$ groups with respect to $CH_3$ groups. In chondrites, we essentially observe the synchronous evolution of chemical and structural characteristics in the transition from TI to TII groups (the exceptions are Bells, Essebi, MIL 0770, whose Raman and IR data point to different groups; Quirico et al., 2018) (Fig. 8). This evolution suggests that the temperature increase is very rapid, promoting chemical and structural reorganization at the same time. In shock experiments, the high pressure conditions last a few μs, while in natural conditions they last longer, from ms to seconds (Beck et al., 2005; Miyahara et al., 2021). However, as pointed out before, a heating time of a few milliseconds to seconds, though longer by several order of magnitudes compared to a μs, remains very short in terms of the kinetics of carbonization and does not explain the difference between experiments and natural samples. The explanation certainly lies in the post-shock time–temperature history, which is very different in the case of natural shocks. Depending on the relative sizes of the impactor and the target, the size of the fragments generated by the collision, and whether they are directly expelled or buried into a regolith that formed from the accumulation of ejecta, the cooling time of a given fragment can vary from minutes to days or even years (Nakato et al., 2008; Stöffler et al., 1991). The geological settling appears as a major actor of short-duration metamorphism, which well accounts for the variety of

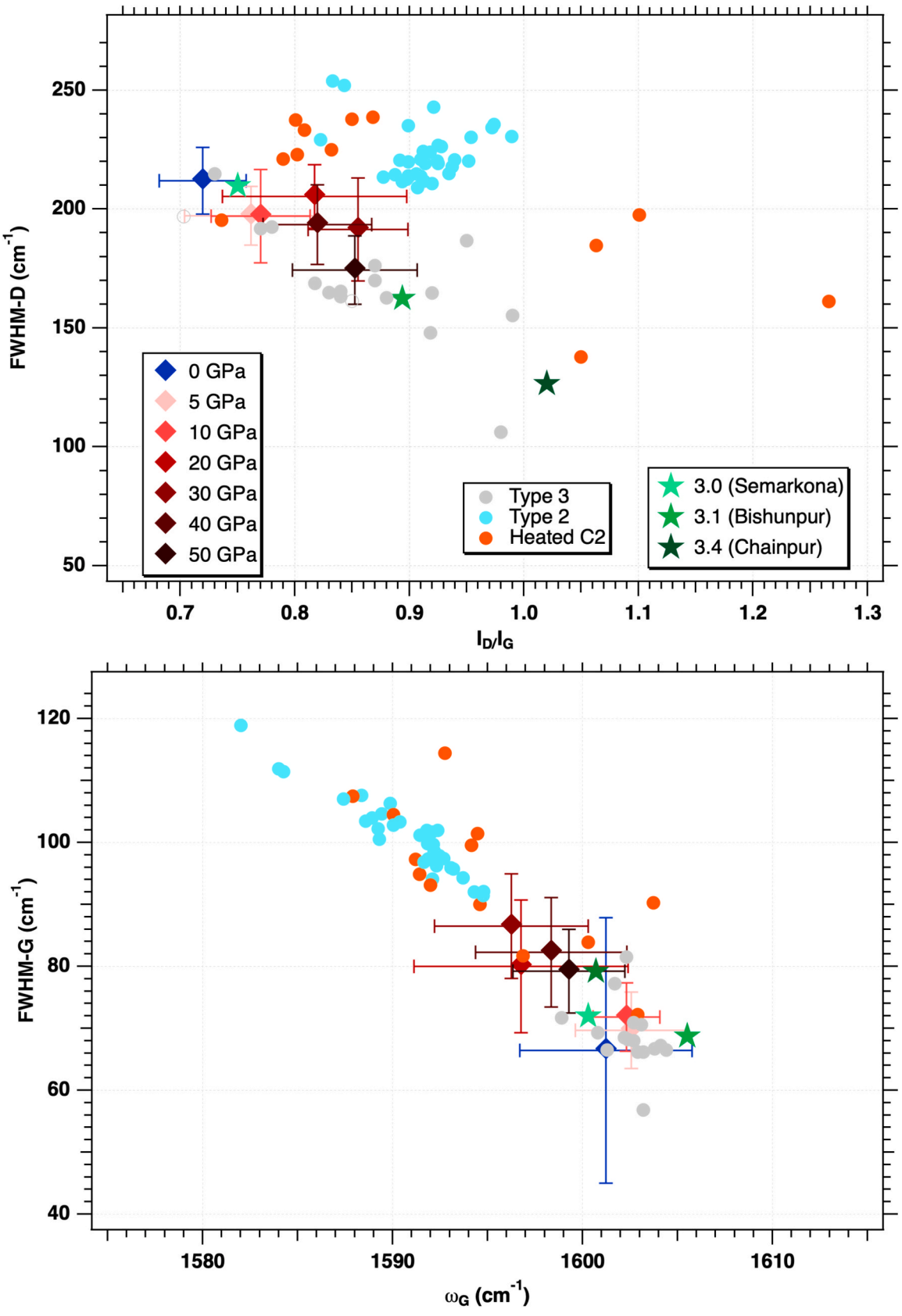


**Fig. 11.** QUE 90628 shocked samples compared with type 2 and type 3 samples, taken from Quirico et al. (2018) and Bonal et al. (2016).

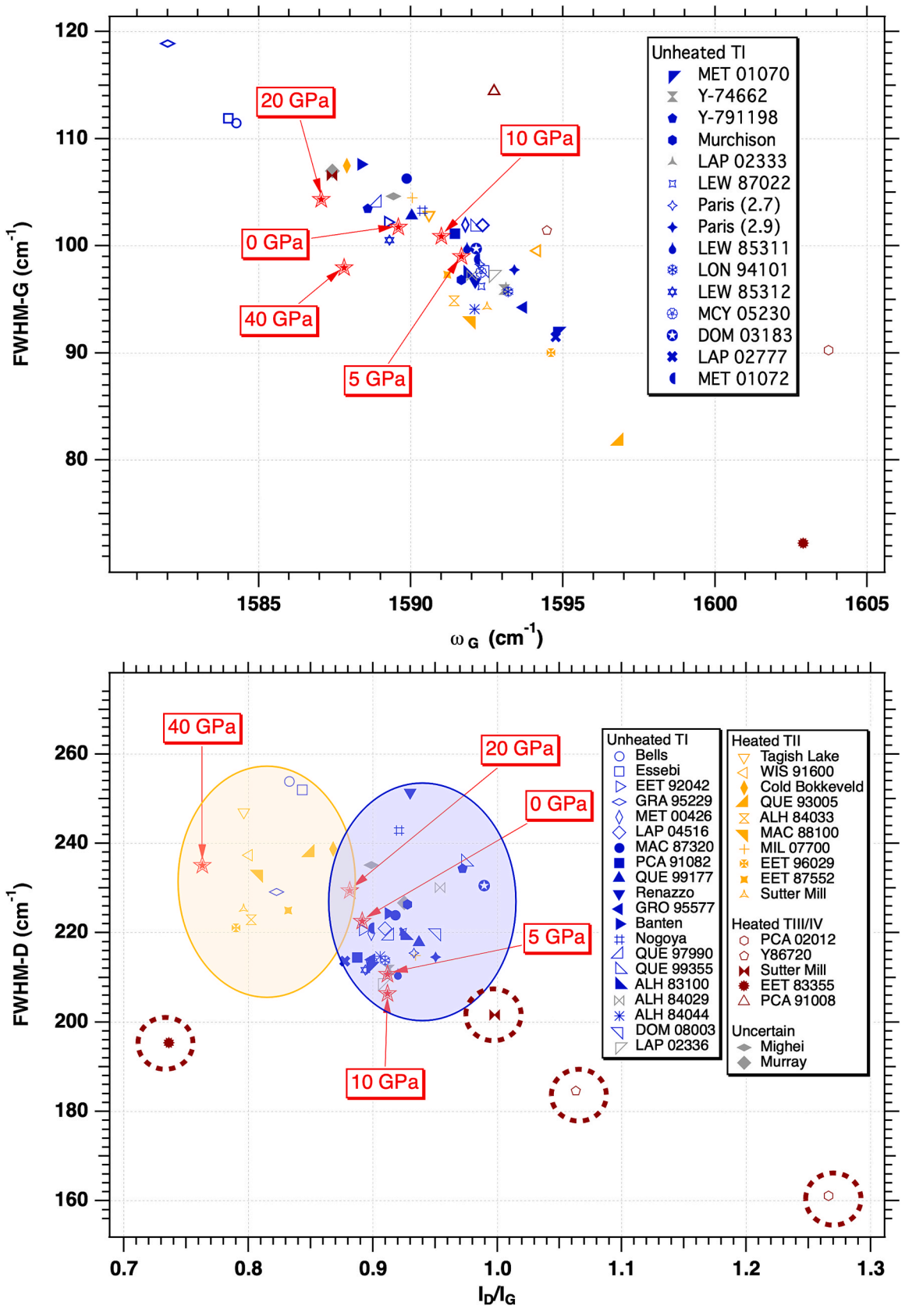


**Fig. 12.** Comparison of the Raman spectral parameters between chondrites and shocked Murchison samples.

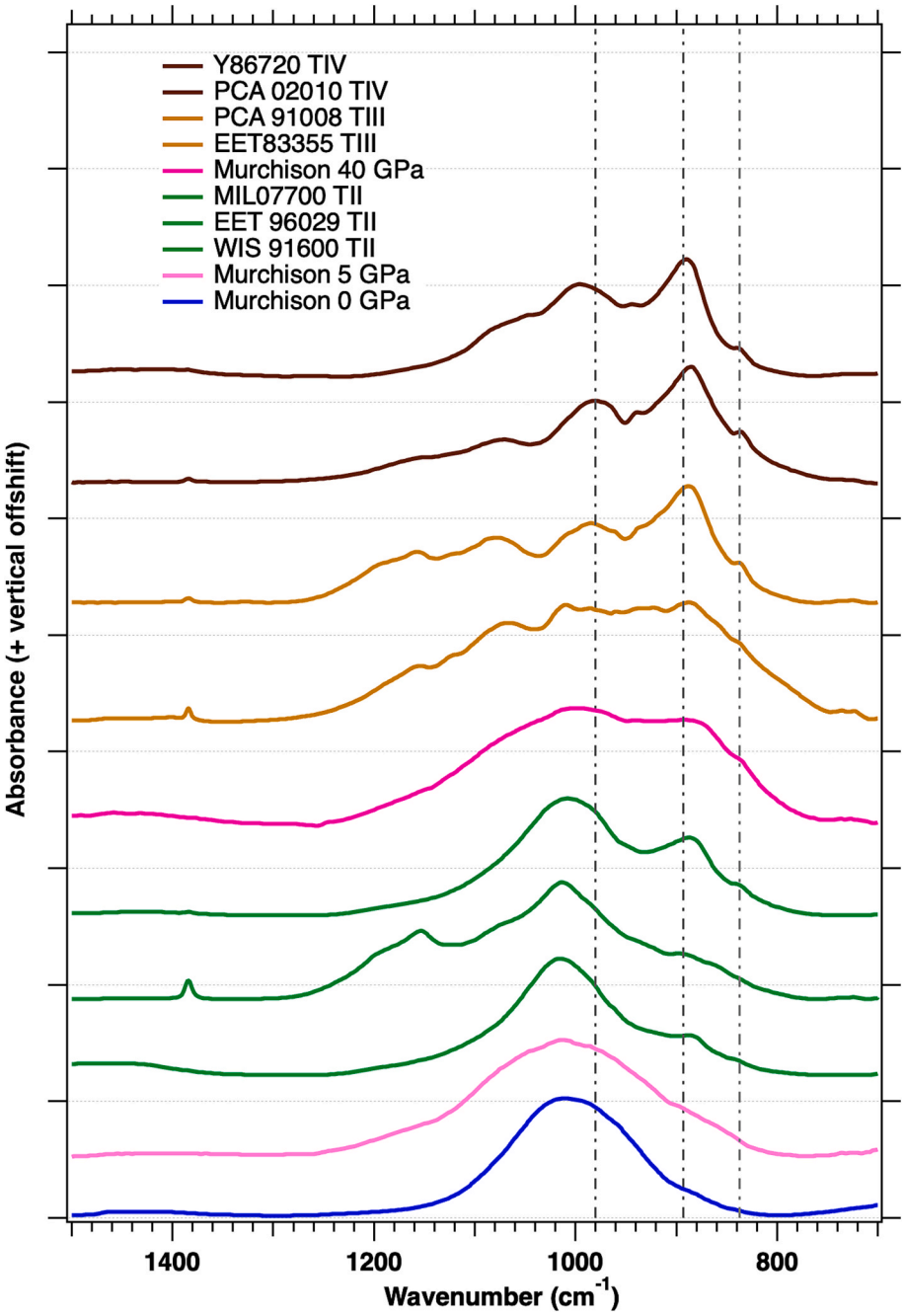


**Fig. 13.** Infrared spectra of bulk chondrites (Beck et al., 2014) compared to matrix grains of shocked Murchison at 5 and 40 GPa. At 40 GPa, the spectrum is between the stages II and III.

lithologies observed in some recent falls (Alexander et al., 2014; Herd et al., 2011; Zolensky et al., 2014). Shock recovery and flash heating experiments are not long enough to reproduce the structural modifications of IOM observed in TIII and TIV chondrites. However, they would best simulate the impact of hypervelocity micrometeorites striking the surface of planetary bodies, generating regolith and feeding it with carbonaceous material.

The infrared spectral range 1600–2000 $cm^{-1}$ also displays significant differences with natural samples. As mentioned above, the component at ~ 1650 $cm^{-1}$ in shocked samples does not exist in natural samples, and has been putatively assigned to a quinone group. The presence of this group is not due to contamination, either during the shock experiment or during IOM extraction, because its abundance increases with the shock pressure. The abundance of carbonyl groups tend to decrease upon increasing the shock pressure, consistently with a carbonization process. But its evolution is not strictly monotonic, and at 50 GPa some spectra show an intense carbonyl band. Moreover, the IOM display substantial chemical heterogeneities. All these spectral characteristics are not observed in natural samples, nor in organic matter heated in the laboratory. We have no explanation for these differences.

### 4.3. *Isotopic evolution of Murchison IOM*

The isotopic evolution of hydrogen in the IOM of shocked samples is characterized by the disappearance of hot spots, a marked drop in δD between the unshocked and shocked samples at 5 GPa, a slight increase up to 20 GPa, then a very marked drop at 40 GPa. At 40 GPa, δD = -79 ± 18 ‰, and there are no more hot spots. The heating experiments

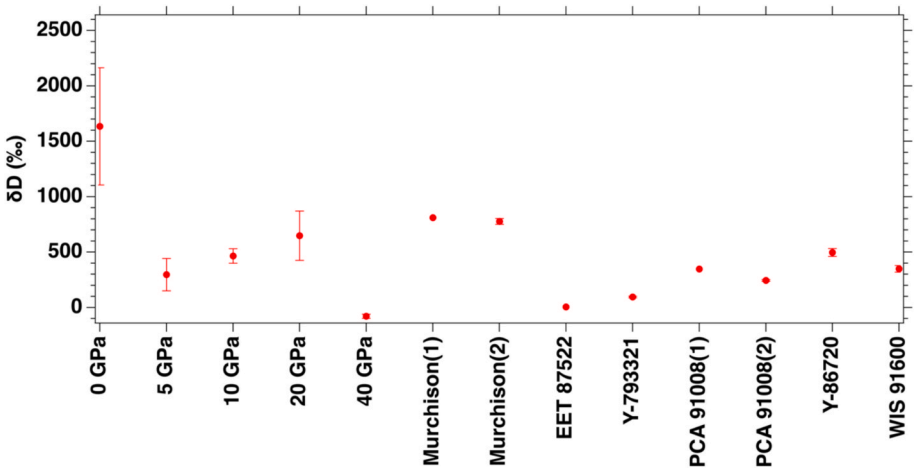


**Fig. 14.** Mean δD (‰) of IOM form shocked samples calculated from the isotope maps (Fig. 8), compared with IRMS measurements on IOM samples extracted from TII (WIS 91600, EET 87522, Y-793321) and TIII/IV heated chondrites (PCA 91008, Y-86720). Data taken from Alexander et al. (2007, 2010).

conducted on the Orgueil IOM (CI) by Remusat et al. (2019) show that samples heated at 300 °C for 1 h show many hot spots, and that the bulk deuteration is higher than in the initial sample (δD = 1200 ± 130 ‰ and 750 ± 130 ‰, respectively). A substantial chemical evolution is also observed: decrease of H/C from 0.67 to 0.12, aliphatic and carbonyl loss. After heating at 500 °C for 1 h, hotspots have completely disappeared and δD = 427 ± 130 ‰. Riebe et al. (2020) report δD variations in the IOM of Cold Bokkeveld (CM) exposed to flash heating experiments (duration 4 s): 725, 871, 661, 604 and 567 ‰ for the unheated sample, 400, 600, 800 and 1000 °C. Even at 1000 °C the bulk deuteration remains high.

The disappearance of hotspots in shocked samples is consistent with these heating experiments. As early as 5 GPa, hotspots have largely disappeared, Nevertheless, a substantial drop of δD is observed in the shock experiments, followed by a slight increase, which is not observed in heating experiments of IOM. But the most striking difference is that, at 40 GPa, a negative δD value is observed. Two explanations can be put forward here. The first is that the above mentioned heating experiments were focused on pure IOM. In the shock experiments, the bulk rock was used, and during the dehydroxylation of serpentines OH and $H_2O$ could interact with IOM and exchange protons. The second is that higher temperature are achieved in the shock experiments.

The comparison with heated chondrites is shown in Fig. 14. The δD values of IOM measured by IRMS analysis are in the range of 81—349 ‰ for TII chondrites, and 347–496 ‰ for TIII/IV chondrites (Alexander et al., 2007, 2010). These values may be underestimates, due to physisorbed molecular water in the samples (Vacher et al., 2020). For Murchison IOM, δD = 777 ± 27 ‰, compared to 1640 ± 530 ‰ in the case of NanoSIMS measurements in our study. The δD values of the IOM in Murchison shocked samples in the 5–20 GPa range, as estimated through NanoSIMS images, are consistent with values in TI and TIII/IV heated chondrites, as measured by IRMS. Note, however, that this comparison should be considered with great care, due to substantial differences between the studies above mentioned. The δD value in the 40 GPa experiment is however much lower, and is inconsistent with all natural samples (Fig. 14). It is important to note that the heated C2 chondrites PCA 91008 and Y-86720 are largely dehydrated, but their bulk δD displays positive values (244–347 ‰ and 496 ‰, respectively), which are much higher than those observed in the 40 GPa experiment. This clearly indicates that the interaction between IOM and $OH/H_2O$ groups during serpentine dehydroxylation was limited.

As mentioned above, the hydration state and the low degree of structural order of IOM in shocked samples are not in agreement with natural samples. Fully dehydrated chondrites (TIII/IV) show a much higher degree of structural order of IOM and they are easily distinguished from TII in the Raman parameters plots (Fig. 12). The temperature–time conditions in the 40 GPa experiment were sufficient to decompose serpentines and release water. But they did not lead to a positive bulk δD value, and they did not promote a substantial degree of $sp^2$ structural order. Finally, the heating process experienced by TIII/IV chondrites is more accurately simulated by conventional heating experiments over hours to days.

## 5. Conclusion

Shock-recovery experiments were carried out on pellets made of Murchison (CM) and EET 90628 (OC L) chondrites. The main conclusions are the following:

- Murchison experiments on bulk Murchison show pyrolysis of aliphatic hydrocarbons and decarboxylation followed by carbonization and oxidation of IOM at all shock intensities (5–50 GPa) and a pronounced structural evolution at 40 GPa associated with complete dehydroxylation of serpentines, along with olivine and glass formation. The δD isotopic composition of IOM evolves significantly, with the rapid disappearance of hot spots and a bulk δD of −79 ‰ is achieved at 40 GPa, compared to 1640 ± 530 ‰ at 0 GPa.
- These experiments only partially reproduce the characteristics of natural samples. The decrease of $I_D/I_G$ in Raman spectra of TII chondrites is reproduced in shock experiments at 40 GPa. However, the presence of olivine is consistent with a stage III of heated type 2 chondrites. In addition, the bulk δD is much lower than that observed in natural samples.
- These results show that the IOM evolution in short-duration heated chondrites is essentially controlled by the post-shock cooling episode, which lasts from hours to years, compared to a few second or minutes in shock experiments. In this respect, the IOM evolution during short-duration heating is better simulated by heating experiments under controlled redox conditions over hours to days.
- Experiments performed on EET 90628 show a structural evolution of IOM consistent with weakly heated natural objects. In particular, the co-evolution of the width and position of the D-band (FWHM-D and $I_D/I_G$, respectively) in the Raman spectra of the shocked samples is consistent with those measured on series of mildly heated type 3 chondrites. However, as observed in the case of Murchison, a substantial increase in IOM structural order, as observed in Ordinary Chondrites with a petrologic type >3.1, is not achieved with shock experiments.
- Due to the very short post-shock heating sequence, shock experiments seem suitable to simulate impacts with small impactors (<

mm), presumably hydrated micrometeorites and cometary grains. This has potential applications to constrain the evolution of the surfaces of airless planetary bodies.

## CRediT authorship contribution statement

**E. Quirico:** Writing – review & editing, Writing – original draft, Visualization, Validation, Supervision, Resources, Project administration, Methodology, Investigation, Funding acquisition, Conceptualization. **H. Yabuta:** Writing – review & editing, Validation, Resources, Methodology, Investigation, Funding acquisition, Conceptualization. **P. Beck:** Writing – review & editing, Validation, Resources, Methodology, Investigation, Funding acquisition, Conceptualization. **L. Bonal:** Writing – review & editing, Validation, Resources, Methodology, Investigation, Data curation, Conceptualization. **A. Bardyn:** Validation, Resources, Methodology, Investigation. **L.R. Nittler:** Writing – review & editing, Validation, Software, Resources, Methodology, Investigation, Formal analysis, Conceptualization. **C.M.O'D. Alexander:** Writing – review & editing, Validation, Resources, Methodology, Investigation, Conceptualization.

## Data availability

The complete spectral datasets (Beck and Potin, 2010; Quirico and Bonal, 2010 and Quirico 2010) presented in the present paper are available online in the GhoSST database on the SSHADE database infrastructure (https://www.sshade.eu/): https://www.sshade.eu/data/experiment/EXPERIMENT_LB_20240904_001. https://www.sshade.eu/data/experiment/EXPERIMENT_LB_20240821_001. https://www.sshade.eu/data/EXPERIMENT_LB_20250307_001.

## Declaration of competing interest

The authors declare that they have no known competing financial interests or personal relationships that could have appeared to influence the work reported in this paper.

## Acknowledgements

This work has been funded by the Centre National d'Etudes Spatiales (CNES-France). We warmly thank Tokyo Institute of Technology (formerly Tokyo Tech) where shock experiments were performed under the guidance of Professor Atou. We acknowledge the Raman facility in ENS-Lyon, supported by the Institut National des Sciences de l'Univers (INSU). We thank the following institutes that provided us with precious meteorite samples: Meteorites Working Group (JSC Houston, USA) and Field Museum Chicago. US Antarctic meteorite samples are recovered by the Antarctic Search for Meteorites (ANSMET) program, which has been funded by NSF and NASA, and characterized and curated by the Department of Mineral Sciences of the Smithsonian Institution and Astromaterials Curation Office at NASA Johnson Space Center.

## References

Alexander, C.M.O., Cody, G.D., Kebukawa, Y., Bowden, R., Fogel, M.L., Kilcoyne, A.L.D., Nittler, L.R., Herd, C.D.K., 2014. Elemental, isotopic, and structural changes in Tagish Lake insoluble organic matter produced by parent body processes. Meteorit. Planet. Sci. 49, 503–525.

Alexander, C.M.O., Howard, K.T., Bowden, R., Fogel, M.L., 2013. The classification of CM and CR chondrites using bulk H, C and N abundances and isotopic compositions. Geochim. Cosmochim. Acta 123, 244–260.

Alexander, C.M.O., Newsome, S.D., Fogel, M.L., Nittler, L.R., Busemann, H., Cody, G.D., 2010. Deuterium enrichments in chondritic macromolecular material—implications for the origin and evolution of organics, water and asteroids. Geochim. Cosmochim. Acta 74, 4417–4437.

Anderson, W.W., Ahrens, T.J., 1998. Shock wave equations of state of chondritic meteorites, in: AIP Conference Proceedings. Presented at the The tenth American Physical Society topical conference on shock compression of condensed matter, AIP, Amherst, Massachusetts (USA), pp. 115–118.

Atou, T., Kawai, N., Ito, S., Yubuta, K., Kikuchi, M., 2010. Instantaneous nano-order fragmentation in mullite ceramics triggered by a shock-induced phase transition. J. Appl. Phys. 108, 093523.

Beck, P., Garenne, A., Quirico, E., Bonal, L., Montes-Hernandez, G., Moynier, F., Schmitt, B., 2014. Transmission infrared spectra (2–25μm) of carbonaceous chondrites (CI, CM, CV–CK, CR, C2 ungrouped): mineralogy, water, and asteroidal processes. Icarus 229, 263–277.

Beck, P., Gillet, Ph., El Goresy, A., Mostefaoui, S., 2005. Timescales of shock processes in chondritic and martian meteorites. Nature 435, 1071–1074.

Beck, P., Quirico, E., Montes-Hernandez, G., Bonal, L., Bollard, J., Orthous-Daunay, F.-R., Howard, K.T., Schmitt, B., Brissaud, O., Deschamps, F., Wunder, B., Guillot, S., 2010. Hydrous mineralogy of CM and CI chondrites from infrared spectroscopy and their relationship with low albedo asteroids. Geochim. Cosmochim. Acta 74, 4881–4892.

Bonal, L., Quirico, E., Flandinet, L., Montagnac, G., 2016. Thermal history of type 3 chondrites from the Antarctic meteorite collection determined by Raman spectroscopy of their polyaromatic carbonaceous matter. Geochim. Cosmochim. Acta 189, 312–337.

Bottke, W. F., Brož, M., O'Brien, D.P., Campo Bagatin, A., Morbidelli, A., Marchi, S., 2015. The Collisional Evolution of the Main Asteroid Belt. In: Michel, P., DeMeo, F. E., Bottke, William F. (Eds.), Asteroids IV. University of Arizona Press.

Chan, Q.H.S., Nakato, A., Kebukawa, Y., Zolensky, M.E., Nakamura, T., Maisano, J.A., Colbert, M.W., Martinez, J.E., Kilcoyne, A.L.D., Suga, H., Takahashi, Y., Takeichi, Y., Mase, K., Wright, I.P., 2019. Heating experiments of the Tagish Lake meteorite: investigation of the effects of short-term heating on chondritic organics. Meteorit. Planet. Sci. 54, 104–125.

Chen, C., Smallwood, J.L., Martin, R.G., Livio, M., 2019. Late delivery of nitrogen to the Earth. Astron. J. 157, 80.

Cody, G.D., Alexander, C.M.O., Tera, F., 2002. Solid-state (1 H and 13 C) nuclear magnetic resonance spectroscopy of insoluble organic residue in the Murchison meteorite: a self-consistent quantitative analysis. Geochim. Cosmochim. Acta 66, 1851–1865.

Cody, G.D., Ade, H., Alexander, C.M.O'.D., Araki, T., Butterworth, A., Fleckenstein, H., Flynn, G., Gilles, M.K., Jacobsen, C., Kilcoyne, A.L.D., Messenger, K., Sandford, S.A., Tyliszczak, T., Westphal, A.J., Wirick, S., Yabuta, H., 2008. Quantitative organic and light-element analysis of comet 81P/ Wild 2 particles using C-, N-, and O-XANES. Meteor. Planet. Sci. 43, 353–365.

Cody, G.D., Heyinga, E., Alexander, C.M.O'.D., Nittler, L.R., Kilcoyne, A.L.D., Sandford, S.A., Stroud, R.M., 2011. Establishing a molecular relationship between chondritic and cometary organic solids. The Proceedings of the National Academy of Sciences 108, 19171–19176.

Eschrig, J., 2022. An investigation of the hydration history of chondrites and search for their asteroidal parent bodies. Cosmology and Extra-Galactic Astrophysics [astro-ph.CO]. Université Grenoble Alpes [2020-..], 2022. English. NNT : 2022GRALU026.. . tel-03999194.

Fritz, J., Greshake, A., Fernandes, V.A., 2017. Revising the shock classification of meteorites. Meteorit. Planet. Sci. 52, 1216–1232.

Furuichi, H., Ujiie, K., Kouketsu, Y., Saito, T., Tsutsumi, A., Wallis, S., 2015. Vitrinite reflectance and Raman spectra of carbonaceous material as indicators of frictional heating on faults: constraints from friction experiments. Earth Planet. Sci. Lett. 424, 191–200.

Garenne, A., Beck, P., Montes-Hernandez, G., Chiriac, R., Toche, F., Quirico, E., Bonal, L., Schmitt, B., 2014. The abundance and stability of "water" in type 1 and 2 carbonaceous chondrites (CI, CM and CR). Geochim. Cosmochim. Acta 137, 93–112.

Herd, C.D.K., Blinova, A., Simkus, D.N., Huang, Y., Tarozo, R., Alexander, C.M.O., Gyngard, F., Nittler, L.R., Cody, G.D., Fogel, M.L., Kebukawa, Y., Kilcoyne, A.L.D., Hilts, R.W., Slater, G.F., Glavin, D.P., Dworkin, J.P., Callahan, M.P., Elsila, J.E., De Gregorio, B.T., Stroud, R.M., 2011. Origin and evolution of prebiotic organic matter as inferred from the Tagish Lake Meteorite. Science 332, 1304–1307.

Howard, K.T., Benedix, G.K., Bland, P.A., Cressey, G., 2011. Modal mineralogy of CM chondrites by X-ray diffraction (PSD-XRD): Part 2. Degree, nature and settings of aqueous alteration. Geochim. Cosmochim. Acta 75, 2735–2751.

Hongo, T., Nakamura, K.G., Atou, T., Kikuchi, M., Yubuta, K., Itoh, S., Kusaba, K., Fukuoka, K., Kondo, K., 2007. Phase transition of Mn F 2 driven by shock compression at pressure of up to 33 GPa. Phys. Rev. B 76.

Hu, J., Sharp, T.G., 2022. Formation, preservation and extinction of high-pressure minerals in meteorites: temperature effects in shock metamorphism and shock classification. Prog. Earth Planet. Sci. 9, 6.

Ibarra, JoséV, Muñoz, E., Moliner, R., 1996. FTIR study of the evolution of coal structure during the coalification process. Org. Geochem. 24, 725–735.

Ikeda, Y., 1992. Ikeda92_ProcNIPR.pdf. Proc NIPR Symp Antarct Meteor. 5, 49–73.

Kaneki, S., Hirono, T., 2018. Kinetic effect of heating rate on the thermal maturity of carbonaceous material as an indicator of frictional heat during earthquakes. Earth Planets Space 70, 92.

Kaneki, S., Ichiba, T., Hirono, T., 2018. Mechanochemical effect on maturation of carbonaceous material: implications for thermal maturity as a proxy for temperature in estimation of coseismic slip parameters. Geophys. Res. Lett. 45, 2248–2256.

Kebukawa, Y., Alexander, C.M.O., Cody, G.D., 2011. Compositional diversity in insoluble organic matter in type 1, 2 and 3 chondrites as detected by infrared spectroscopy. Geochim. Cosmochim. Acta 75, 3530–3541.

Kilcoyne, A.L.D., Tyliszczak, T., Steele, W.F., Fakra, S., Hitchcock, P., Franck, K., Anderson, E., Harteneck, B., Rightor, E.G., Mitchell, G.E., Hitchcock, A.P., Yang, L., Warick, T., Ade, H., 2003. Interferometer controlled scanning transmission microscopes at the advanced light source. J. Synchrotron Rad. 10, 125–136.

Lambrechts, M., Morbidelli, A., Jacobson, S.A., Johansen, A., Bitsch, B., Izidoro, A., Raymond, S.N., 2019. Formation of planetary systems by pebble accretion and

migration: how the radial pebble flux determines a terrestrial-planet or super-Earth growth mode. Astron. Astrophys. 627, A83.
Lievens, C., Ci, D., Bai, Y., Ma, L., Zhang, R., Chen, J.Y., Gai, Q., Long, Y., Guo, X., 2013. A study of slow pyrolysis of one low rank coal via pyrolysis–GC/MS. Fuel Process. Technol. 116, 85–93.
Lin-Vien, D. (Ed.), 1991. The Handbook of Infrared and Raman Characteristic Frequencies of Organic Molecules. Academic Press, Boston.
MacPhail, R.A., Strauss, H.L., Snyder, R.G., Elliger, C.A., 1984. C-H stretching modes and the structure of n-alkyl chains. 2. Long, all-trans chains. J. Phys. Chem. 88, 8.
Mahan, B., Moynier, F., Beck, P., Pringle, E.A., Siebert, J., 2018. A history of violence: insights into post-accretionary heating in carbonaceous chondrites from volatile element abundances, Zn isotopes and water contents. Geochim. Cosmochim. Acta 220, 19–35.
Marsh, S.P., 1980. LASL shock hugoniot data. University of California Press.
Martinez, I., Deutsch, A., Schärer, U., Ildefonse, P., Guyot, F., Agrinier, P., 1995. Shock recovery experiments on dolomite and thermodynamical calculations of impact induced decarbonation. J. Geophys. Res. Solid Earth 100, 15465–15476.
Matsui, T., Osako, M., 1979. Thermal property measurement of Yamato meteorites. Proceedings of the Fourth Symposium on Antarctic Meteorites 243-252.
Matsuoka, K., Nakamura, T., Nakamuta, Y., Takaoka, N., 1996. Matsuoka96_ProcNIPR.pdf 9, 20–36.
Milton, D.J., DeCarli, P.S., 1989. Maskelynite: formation by explosive shock. Science 140, 670–671.
Mimura, K., Arao, T., Sugiura, M., Sugisaki, R., 2003. Shock-induced carbonization of phenanthrene at pressures of 7.9–32 GPa. Carbon 41, 2547–2553.
Mimura, K., Okamoto, M., Nakatsuka, T., Sugitani, K., Abe, O., 2005. Shock-induced isotope evolution of hydrogen and carbon in meteorites. Geophys. Res. Lett. 32, 2005GL023050.
Mitchell, A.C., Nellis, W.J., 1981. Shock compression of aluminum, copper, and tantalum. J. Appl. Phys. 52, 3363–3374.
Miyahara, M., Edanaga, J., Yamaguchi, A., Kobayashi, T., Sekine, T., Nakamura, A., 2021. Chondrule flattening by shock recovery Experiments on unequilibrated chondrites. J. Geophys. Res. Planets 126, e2021JE006864.
Muirhead, D.K., Parnell, J., Taylor, C., Bowden, S.A., 2012. A kinetic model for the thermal evolution of sedimentary and meteoritic organic carbon using raman spectroscopy. J. Anal. Appl. Pyrolysis 96, 153–161.
Nachenius, R.W., Ronsse, F., Venderbosch, R.H., Prins, W., 2013. Biomass pyrolysis. Adv. Chemical Engineering. Elsevier 75–139.
Nakamura, T., 2005. Post-hydration thermal metamorphism of carbonaceous chondrites. J. Mineral. Petrol. Sci. 100, 260–272.
Nakamura, T., 2000. Impact-induced textural changes of CV Carbonaceous chondrites: experimental reproduction. Icarus 146, 289–300.
Nakato, A., Nakamura, T., Kitajima, F., Noguchi, T., 2008. Evaluation of dehydration mechanism during heating of hydrous asteroids based on mineralogical and chemical analysis of naturally and experimentally heated CM chondrites. Earth Planets Space 60, 855–864.
Okumura, F., Mimura, K., 2011. Gradual and stepwise pyrolyses of insoluble organic matter from the Murchison meteorite revealing chemical structure and isotopic distribution. Geochim. Cosmochim. Acta 75, 7063–7080.
Opeil, C.P., Britt, D.T., Macke, R.J., Consolmagno, G.J., 2020. The surprising thermal properties of CM carbonaceous chondrites. Meteorit. Planet. Sci. 55, maps.13556.
Orthous-Daunay, F.-R., Quirico, E., Beck, P., Brissaud, O., Dartois, E., Pino, T., Schmitt, B., 2013. Mid-infrared study of the molecular structure variability of insoluble organic matter from primitive chondrites. Icarus 223, 534–543.
Painter, P.C., Snyder, R.W., Starsinic, M., Coleman, M.M., Kuehn, D.W., Davis, A., 1981. Concerning the application of FT-IR to the study of coal: a critical assessment of band assignments and the application of spectral analysis programs. Appl. Spectrosc. 35, 475–485.
Péron, S., Moreira, M., Agranier, A., 2018. Origin of light noble gases (He, Ne, and Ar) on earth: a review. Geochem. Geophys. Geosystems 19, 979–996.
Petersen, H.I., Rosenberg, P., Nytoft, H.P., 2008. Oxygen groups in coals and alginite-rich kerogen revisited. Int. J. Coal Geol. 74, 93–113.
Piqueux, S., Vu, T.H., Bapst, J., Garvie, L.A.J., Choukroun, M., Edwards, C.S., 2021. Specific heat capacity measurements of selected meteorites for planetary surface temperature modeling. J. Geophys. Res. Planets 126, e2021JE007003.
Potin, S., Brissaud, O., Beck, P., Schmitt, B., Magnard, Y., Correia, J.-J., Rabou, P., Jocou, L., 2018. SHADOWS: a spectro-gonio radiometer for bidirectional reflectance studies of dark meteorites and terrestrial analogs: design, calibrations, and performances on challenging surfaces. Appl. Opt. 57, 8279.
Quirico, E., Bonal, L., Beck, P., Alexander, C.M.O., Yabuta, H., Nakamura, T., Nakato, A., Flandinet, L., Montagnac, G., Schmitt-Kopplin, P., Herd, C.D.K., 2018. Prevalence and nature of heating processes in CM and C2-ungrouped chondrites as revealed by insoluble organic matter. Geochim. Cosmochim. Acta 241, 17–37.
Quirico, E., Orthous-Daunay, F.-R., Beck, P., Bonal, L., Brunetto, R., Dartois, E., Pino, T., Montagnac, G., Rouzaud, J.-N., Engrand, C., Duprat, J., 2014. Origin of insoluble organic matter in type 1 and 2 chondrites: new clues, new questions. Geochim. Cosmochim. Acta 136, 80–99.
Remusat, L., Bonnet, J.-Y., Bernard, S., Buch, A., Quirico, E., 2019. Molecular and isotopic behavior of insoluble organic matter of the Orgueil meteorite upon heating. Geochim. et Cosmochim Acta 263, 235–247.
Riebe, M.E.I., Foustoukos, D.I., Alexander, C.M.O'D., Steele, A., Cody, G.D., Mysen, B.O., Nittler, L.R., 2020. The effects of atmospheric entry heating on organic matter in interplanetary dust particles and micrometeorites. Earth Planet. Sci. Lett. 540, 116266.
Schmitt, R.T., Deutsch, A., Stöffler, D., 1994. Calculation of hugoniot curves and post-shock temperatures for H- and L-chondrites. Lunar Planet. Sci. Conf. LPSC XXV.
Scott, E.R., Keil, K., Stoeffler, D., 1992. Shock metamorphism of carbonaceous chondrites. Geochim. Cosmochim. Acta 56, 4281–4293.
Stern, S.A., Kenyon, S.J., 2003. Collisions, accretion, and erosion in the Kuiper Belt. Comptes Rendus Phys. 4, 803–808.
Stöffler, D., 1972. Deformation and transformation of rock-forming minerals by natural and experimental shock processes. Fortschr Min. 49.
Stöffler, D., Hamann, C., Metzler, K., 2018. Shock metamorphism of planetary silicate rocks and sediments: proposal for an updated classification system. Meteorit. Planet. Sci. 53, 5–49.
Stöffler, D., Keil, K., Edward, R.D.S., 1991. Shock metamorphism of ordinary chondrites. Geochim. Cosmochim. Acta 55, 3845–3867.
Stöffler, D., Langenhorst, F., 1994. Shock metamorphism of quartz in nature and experiment: I. basic observation and theory*. Meteoritics 29, 155–181.
Thomas, S.A., Hixson, R.S., Hawkins, M.C., Strand, O.T., 2019. Wave speeds in single and polycrystalline copper 15.
Tomeoka, K., 1990. Mineralogy and petrology of Belgica-7904: a new kind of carbonaceous chondrite from Antarctica. Proc. NIPR Symp. Antarct Meteor. 3, 40–54.
Tomeoka, K., Kojima, H., Yanai, K., 1989a. YAMAT0-86720: a CM carbonaceous chondrite having experienced extensive aqueous alteration and thermal metamorphism. Proc. NIPR Symp. Antarct. Meteor. 2, 55–74.
Tomeoka, K., KonMA, H., Yanai, K., 1989b. YAMAT0-82162: a new kind of ci carbonaceous chondrite found in Antarctica. Proc NIPR Symp Antarct Meteor. 2, 36–54.
Tomeoka, K., Yamahana, Y., Sekine, T., 1999. Experimental shock metamorphism of the Murchison CM carbonaceous chondrite. Geochim. Cosmochim. Acta 63, 3683–3703.
Tomioka, N., Tomeoka, K., Nakamura-Messenger, K., Sekine, T., 2007. Heating effects of the matrix of experimentally shocked Murchison CM chondrite: comparison with micrometeorites. Meteorit. Planet. Sci. 42, 19–30.
Tonui, E., Zolensky, M., Hiroi, T., Nakamura, T., Lipschutz, M.E., Wang, M.-S., Okudaira, K., 2014. Petrographic, chemical and spectroscopic evidence for thermal metamorphism in carbonaceous chondrites I: CI and CM chondrites. Geochim. Cosmochim. Acta 126, 284–306.
Tonui, E., Zolensky, M., Lipschutz, M., 2002. Petrography, mineralogy and trace element chemistry of Yamato-86029, Yamato-793321 and Lewis Cliff 85332: aqueous alteration and heating events. Antarct Meteor. Res 15, 38–58.
Tonui, E.K., Zolensky, M.E., Lipschutz, M.E., Wang, M., Nakamura, T., 2003. Yamato 86029: aqueously altered and thermally metamorphosed CI-like chondrite with unusual textures. Meteorit. Planet. Sci. 38, 269–292.
Tyburczy, J.A., Frisch, B., Ahrens, T.J., 1986. Shock-induced volatile loss from a carbonaceous chondrite: implications for planetary accretion. Earth Planet. Sci. Lett. 80, 201–207.
Vacher, L.G., Piani, L., Rigaudier, T., Thomassin, D., Florin, G., Piralla, M., Marrocchi, Y., 2020. Hydrogen in chondrites: influence of parent body alteration and atmospheric contamination on primordial components. Geochim. Et Cosmochim. Acta 281, 53–66.
Wang, M.-S., Lipschutz, M.E., 1998. Thermally metamorphosed carbonaceous chondrtites from data for thermally mobile elements. Meteorit. Planet. Sci. 33, 1297–1302.
Weber, J.N., Greer, R.T., 1965. Dehydration of serpentine: heat of reaction and reaction keinetics at pH2O=1 atm. Am. Mineral. 50.
Zolensky, M., Mikouchi, T., Fries, M., Bodnar, R., Jenniskens, P., Yin, Q., Hagiya, K., Ohsumi, K., Komatsu, M., Colbert, M., Hanna, R., Maisano, J., Ketcham, R., Kebukawa, Y., Nakamura, T., Matsuoka, M., Sasaki, S., Tsuchiyama, A., Gounelle, M., Le, L., Martinez, J., Ross, K., Rahman, Z., 2014. Mineralogy and petrography of C asteroid regolith: the Sutter's Mill CM meteorite. Meteorit. Planet. Sci. 49, 1997–2016.
Zolensky, M.E., Bourcier, W.L., Gooding, J.L., 1989. Aqueous alteration on the hydrous asteroids: results of EQ3/6 computer simulations. Icarus 78, 411–425.